



## OPEN ACCESS

EDITED BY  
Hu Wang,  
Southwest Jiaotong University, China

REVIEWED BY  
Xu Zhao,  
Guangzhou Institute of Geochemistry  
(CAS), China  
Yong Wang,  
Chengdu University of Technology,  
China

\*CORRESPONDENCE  
Zhiming Yang,  
✉ zm.yang@hotmail.com  
Huawen Cao,  
✉ caohuawen1988@126.com

SPECIALTY SECTION  
This article was submitted to  
Structural Geology and Tectonics,  
a section of the journal  
Frontiers in Earth Science

RECEIVED 21 November 2022  
ACCEPTED 14 December 2022  
PUBLISHED 06 January 2023

CITATION  
Dai Z, Yang Z, Li G, Xie Y, Dong L, Gao K  
and Cao H (2023), Partial melting of  
amphibolitic lower crust and  
subsequent melt-crystal separation for  
generation of the Early Eocene  
magmatism in eastern Himalaya.  
*Front. Earth Sci.* 10:1104197.  
doi: 10.3389/feart.2022.1104197

COPYRIGHT  
© 2023 Dai, Yang, Li, Xie, Dong, Gao and  
Cao. This is an open-access article  
distributed under the terms of the  
[Creative Commons Attribution License  
\(CC BY\)](https://creativecommons.org/licenses/by/4.0/). The use, distribution or  
reproduction in other forums is  
permitted, provided the original  
author(s) and the copyright owner(s) are  
credited and that the original  
publication in this journal is cited, in  
accordance with accepted academic  
practice. No use, distribution or  
reproduction is permitted which does  
not comply with these terms.

# Partial melting of amphibolitic lower crust and subsequent melt-crystal separation for generation of the Early Eocene magmatism in eastern Himalaya

Zuowen Dai<sup>1</sup>, Zhiming Yang<sup>1,2\*</sup>, Guangming Li<sup>3</sup>, Yuling Xie<sup>1</sup>,  
Lei Dong<sup>3</sup>, Ke Gao<sup>3</sup> and Huawen Cao<sup>3\*</sup>

<sup>1</sup>School of Civil and Resource Engineering, University of Science and Technology Beijing, Beijing, China, <sup>2</sup>Institute of Geology, Chinese Academy of Geological Sciences, Beijing, China, <sup>3</sup>Chengdu Center, China Geological Survey, Chengdu, China

The Himalayan leucogranites provide a good opportunity to investigate the crustal evolution of the southern Qinghai-Tibet Plateau. In this study, we present zircon U-Pb and monazite U-Th-Pb ages, zircon Hf isotopes and whole-rock Sr-Nd-Pb isotopes and major and trace elements for the Liemai two-mica granite, eastern Himalaya. Together with previously published data we revalued the petrogenesis of the Early Eocene magmatic rocks in this region and their geological implications. The zircon and monazite U-(Th)-Pb dating results showed that the Liemai two-mica granite was generated at ~ 43 Ma, similar to adjacent Yardoi, Dala and Quedang adakitic two-mica granites, Ridang subvolcanic rocks and Yardoi leucogranite. The Liemai two-mica granite, similar to these coeval adakitic two-mica granites, is enriched in SiO<sub>2</sub>, Al<sub>2</sub>O<sub>3</sub>, Th, U, Pb, La, and Sr, and depleted in MgO, total iron, Yb and Y with high Sr/Y and (La/Yb)<sub>N</sub> ratios (showing adakitic affinities), and exhibits enriched Sr-Nd-Pb-Hf isotopic compositions, suggesting an origin of a thickened lower crust consisting mainly of garnet amphibolite. Although the Ridang subvolcanic rocks and Yardoi leucogranite show similar Sr-Nd-Hf isotopes to these adjacent coeval two-mica granites, perceptible differences in whole-rock major and trace elements can be observed. Broadly, these granites can be divided into high-Mg# granites (HMGs, the two-mica granites) and low-Mg# granites (LMGs, the Ridang subvolcanic rocks and Yardoi leucogranite). The former has relatively higher contents of total iron, MgO, Mg#, TiO<sub>2</sub>, P<sub>2</sub>O<sub>5</sub>, LREE, Y, Th, Sr, incompatible elements (Cr and Ni) and Eu/Eu\* values, and lower contents of SiO<sub>2</sub> and Rb/Sr and Rb/Ba ratios, thus is less evolved than the latter. According to recent studies of differentiation processes in silicic magma reservoirs, we proposed that the HMGs represent a congealed crystal mush that was composed of 'cumulate crystals' and a trapped interstitial liquid, while the LMGs represent the almost pure liquid that was extracted from the crystal mush. Modeling using the trace elements Sr and Ba shows that the extraction probably occurred when the crystallinity of the mush was ~ 60%–63%, at least for the most evolved LMGs sample. The HMGs correspond to a residual crystal mush that had a terminal porosity of ~ 21%–25%

filled with a trapped interstitial liquid. Underplating of mafic magmas following slab breakoff of the Neo-Tethys oceanic lithosphere caused partial melting of the amphibolitic lower crust, which had been thickened to 50 km prior to 43 Ma.

#### KEYWORDS

adakitic rocks, crystal mush, melt-crystal separation, crustal thickening, Liemai, Himalaya

## 1 Introduction

Magma is an important carrier for material and energy exchange among inner spheres of our planet (Mo et al., 2007; Yang et al., 2015a; Yang et al., 2015b; Yang et al., 2016a; Zheng et al., 2016; Cao et al., 2022a). Magmatic rocks are regarded as a “probe” for exploring the deep Earth, and carry crucial information for crustal evolution, plate movement and tectonic events (Mo et al., 2007; Zhu et al., 2009a; Mo, 2011; Hou et al., 2015; Li et al., 2020). It is noteworthy that significant breakthroughs have been made in qualitative and even quantitative estimation for crustal thickness in ancient orogens using some geochemical indices of intermediate-felsic magmatic rocks or accessory minerals therein (Profeta et al., 2015; Hu et al., 2017; Tang et al., 2020; Luffi and Ducea, 2022). For example, magmatic rocks with high Sr/Y and (La/Yb)<sub>N</sub> ratios, i.e., adakites or adakitic rocks (Martin, 1986; Defant and Drummond, 1990), are typically considered as prototypical products of high pressure condition, thus indicating an abnormally thick crust (>50 km) (Xu et al., 2002; Chung et al., 2003; Dai et al., 2020a; 2020b; Zeng et al., 2020). The theoretical basis for this crustal thickness estimation is the pressure-dependent behavior of Sr, Y, La, and Yb during partial melting of lower crustal mafic rocks (or their metamorphic equivalents) and fractionation of mantle-derived mafic magmas in the lower crust. At low pressure (<~1.0 GPa), Sr preferentially incorporates into plagioclase, whereas Y and Yb still remain in the melt, resulting in low Sr/Y and La/Yb ratios in the melt. However, at high pressure (>~1.0 GPa), Y and Yb preferentially partitions into garnet and amphibole, while Sr and La remain in the melt, resulting in melts with high Sr/Y and La/Yb values (Davidson et al., 2007; Moyen, 2009).

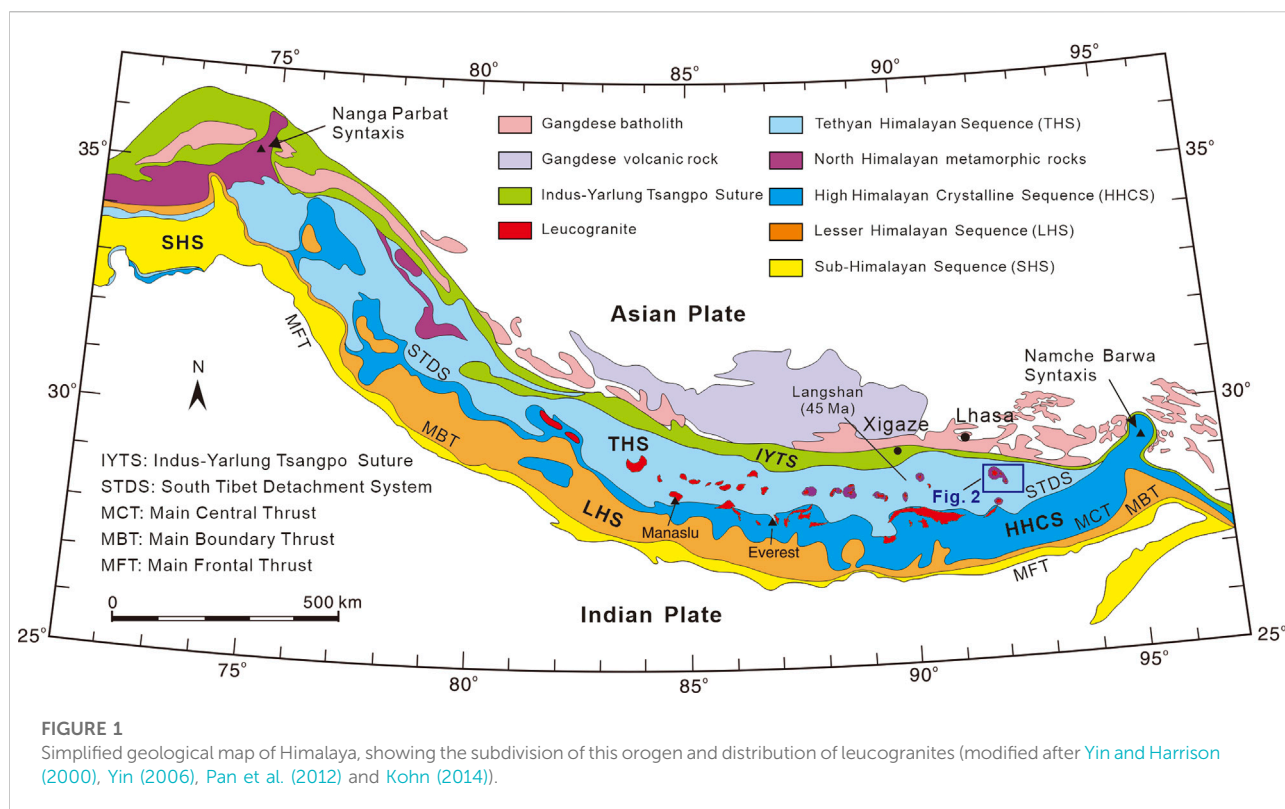
In southern Qinghai-Tibet Plateau, voluminous Cenozoic leucogranites were well developed along the Himalaya orogenic belt forming a 2,000 km-long west-east trending leucogranite belt (Liu et al., 2017; Wu et al., 2020; Cao et al., 2022b). These massive magmatic rocks were formed during the collision between India and Eurasia, thus play a crucial role in exploring the evolution of the orogenic belt (Hou et al., 2012; Wu et al., 2015; Fu et al., 2020; Zhang et al., 2020). For instance, the Early Eocene granites were normally considered as adakitic rocks based on their high Sr/Y ratios, thus were viewed as products of partial melting of a thickened (>50 km) lower crust (Zeng et al., 2011, 2015; Hou et al., 2012; Dai et al., 2020a). However, a recent study proposed that the fractional crystallization (plagioclase accumulation),

rather than melting at the base of the thickened crust, was probably responsible for generation of the high Sr/Y ratios of these adakitic rocks (Gao et al., 2021). Undoubtedly, this novel viewpoint pushes us to rethink the traditional perception for generation of these Early Eocene magmatic rocks as well as the evolutionary history of crust in the Himalayan orogen.

In this study we present monazite U-Th-Pb and zircon U-Pb ages, zircon Hf and whole-rock Sr-Nd-Pb isotopes and whole-rock major and trace elements for two-mica granite exposed in Liemai (village), southeastern Yardoi dome. Together with previously published data we revalued the petrogenesis of the Early Eocene magmatic rocks in this region and their geological implications.

## 2 Geological setting and sample description

Himalaya, the south most component of the Qinghai-Tibet plateau, is the highest and youngest collisional orogen on Earth resulted from collision between India and Asia during Late Cretaceous to Paleocene (Figure 1; Yin and Harrison, 2000; Yin, 2006; Pan et al., 2012; Kohn, 2014). It is bound by the Indus-Yarlung Tsangpo Suture zone in the north from the Lhasa terrane and the Main Frontier Thrust (MFT) in the south from the Indian plate. The Himalaya can be subdivided into the Tethyan Himalayan Sequence (THS), Higher Himalayan Crystalline Sequence (HHCS), Lower Himalayan Sequence (LHS), and the Sub-Himalayan Sequence (SHS) (Figure 1). These subterranean are separated by several north-dipping fault systems, from north to south including the south Tibet detachment system (STDS), the Main Central Thrust (MCT), and the Main Boundary Thrust (MBT) (Figure 1). The STDS represents a normal fault system while the other two are reverse faults (Leloup et al., 2010; Zhang et al., 2012). The THS represents the Indian passive continental margin sedimentary sequences and mainly comprises Late Proterozoic to Mesozoic unmetamorphosed or low-grade metamorphic siliciclastic and carbonate rocks; The HHCS represents a series of Late Proterozoic to Paleozoic metasedimentary sequences (typically upper amphibolite to lower granulite facies) that were derived from the basement of the Indian continent; The LHS represents a suite of Proterozoic low-grade metamorphic rocks (typically greenschist to amphibolite facies); While the SHS represents a series of coarse-grained clastic sediments (Siwalik Group), which

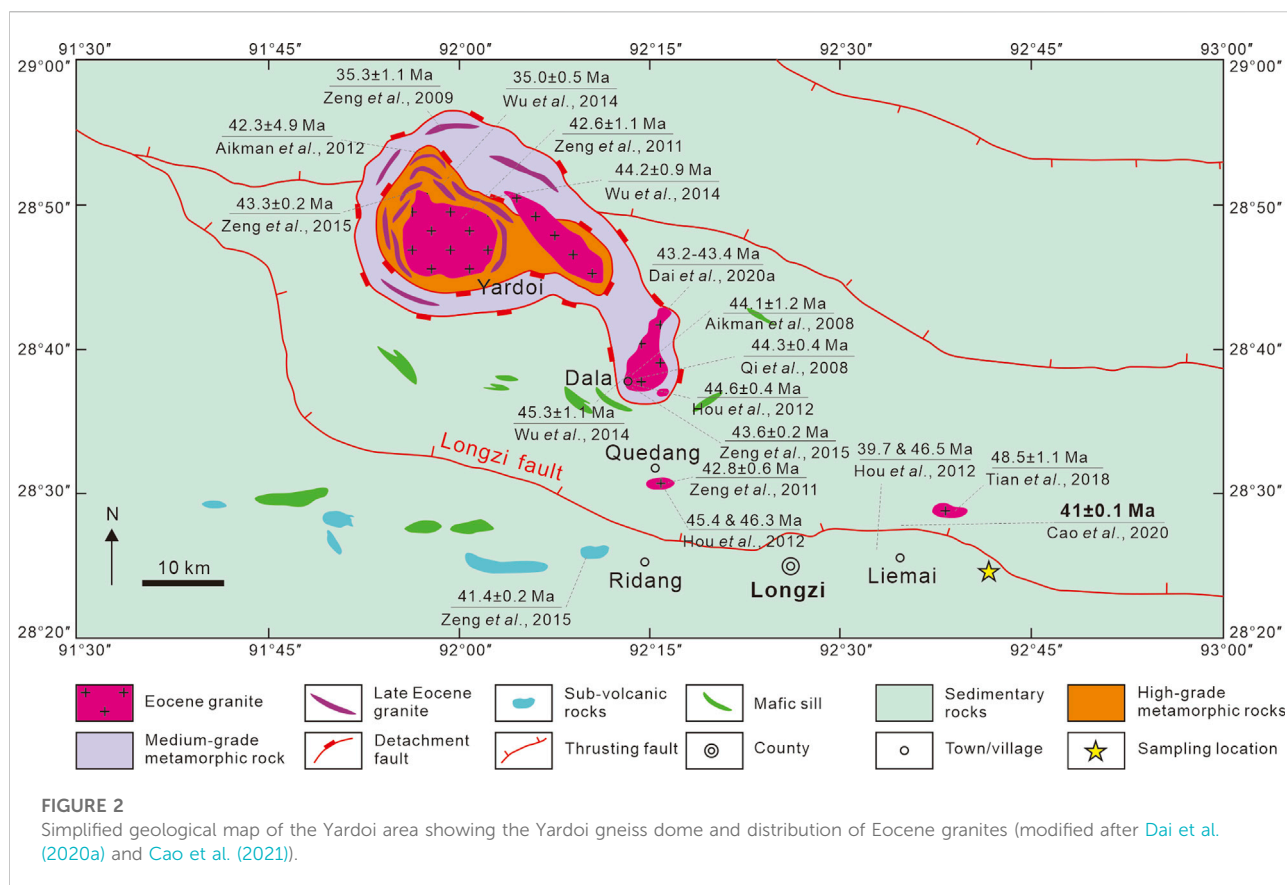


were deposited during foreland molasse sedimentation following the uplift of the Himalaya (Kohn, 2014; Cao et al., 2018; Myrow et al., 2019).

Owing to continuous collision between India and Asia, the Himalayan crust experienced intense and extensive deformation, metamorphism and anatexis, which resulted in formation of voluminous leucogranites. These leucogranites constitute two huge sub-parallel leucogranite belts, i.e. the Tethyan Himalayan leucogranite belt (also known as the North Himalayan leucogranite belt) to the north and the Higher Himalayan leucogranite belt to the south (Figure 1; Wu et al., 2015). Normally, the Higher Himalayan leucogranites were emplaced into the HHCS adjacent to the STDS forming a discontinuous chain of sheets, dykes, sills, and laccolithic bodies (Figure 1; Wu et al., 2015). In contrast, most Tethyan Himalayan leucogranites are exposed in the cores of the north Himalayan gneiss domes, except for a few isolated intrusions and sills that intruded into the THS (such as the Dala and Quedang two-mica granites) (Figure 1; Wu et al., 2015). The Himalayan leucogranites are composed of biotite granite, two-mica granite, muscovite granite, tourmaline granite, and garnet granite, and were emplaced between 48.5 and 0.7 Ma (Wu et al., 2015, 2020; Cao et al., 2022b). Typically, the Miocene leucogranites are considered as highly fractionated (strong) peraluminous S-type granites (Wu et al., 2015, 2020). While the majority of Eocene granites are

characterized by high Sr/Y ratios and, therefore, considered as products of partial melting of a thickened amphibolitic lower crust with minor metapelites (Zeng et al., 2011, 2015; Hou et al., 2012; Dai et al., 2020a).

The Himalayan Eocene granites were mainly exposed in Yardoi (Yalaxiangbo) gneiss dome and areas nearby, occurred as stocks (Yardoi, Dala and Quedang), and dikes or sills (Liema and Ridang) (Figure 2; Zeng et al., 2015; Cao et al., 2022b). The majority of granites in this region were generated in the Early Eocene (Ca. 40–48 Ma; Qi et al., 2008; Aikman et al., 2008, 2012; Zeng et al., 2011, 2015; Hou et al., 2012; Wu et al., 2014; Tian et al., 2018; Dai et al., 2020a; Cao et al., 2020) except for minor that were formed at the Early Eocene (~35 Ma; Zeng et al., 2009; Wu et al., 2014). On the basis of lithologic features, these Early Eocene granites can be divided into two types, i.e., two-mica granite and leucogranite granite (almost without biotite). The former constituted the main part of the Early Eocene granites in Yardoi area, including Yardoi, Dala and Quedang two-mica granite and the majority of adjacent sills (Hou et al., 2012; Zeng et al., 2015; Dai et al., 2020a). While the latter exposed as minor sills or dikes in Yardoi dome (Yardoi leucogranite) or in County Longzi (near Ridang town) (subvolcanic rocks) (Hu et al., 2011b; Zeng et al., 2015). Samples in this study were collected from a sill with a width of 5–8 m that was exposed 10 km away from east of Liema village (GPS: 92°41'44.37", 28°25'12.59"; Figures 2, 3A). The rock (two-mica granite) shows fine-grained



granitic texture and are composed of eu- to subhedral K-feldspar (35–40 vol.%) and plagioclase (30–35 vol.%), anhedral quartz (15–20 vol.%), sub- to anhedral biotite (10–15 vol.%) and muscovite (~5 vol.%), and accessory minerals (zircon, monazite, apatite and titanite). Polysynthetic twinning well-developed in plagioclase. Sericitization is very common in K-feldspar (Figures 3B–F).

### 3 Analytical methods

#### 3.1 Zircon U-Pb dating and Hf isotopes

Rock sample was crushed and washed, followed by conventional heavy-liquid and magnetic separation to separate zircon grains. Representative zircon grains were handpicked under a binocular microscope and then mounted in epoxy resin and polished to a smooth flat surface. Sample processing was conducted at the Langfang Regional Geological Survey (Hebei Province, China). Prior to U-Pb dating, internal features of zircons were observed using transmitted, reflected, and cathodoluminescence images. These images were obtained at the Wuhan Sample Solution Analytical Technology Co., Ltd. (Hubei Province, China).

U-Pb dating and trace element analysis of zircon were simultaneously conducted by LA-ICP-MS at the Wuhan Sample Solution Analytical Technology Co., Ltd. Detailed operating conditions for the laser ablation system and the ICP-MS instrument and data reduction are the same as description by Zong et al. (2017). Laser sampling was performed using a GeolasPro laser ablation system that consists of a COMPexPro 102 ArF excimer laser (wavelength of 193 nm) and a MicroLas optical system. An Agilent 7700e ICP-MS instrument was used to acquire ion-signal intensities. Helium was applied as a carrier gas. Argon was used as the make-up gas and mixed with the carrier gas *via* a T-connector before entering the ICP. A “wire” signal smoothing device is included in this laser ablation system (Hu et al., 2015). The spot size and frequency of the laser were set to 32  $\mu\text{m}$  and 8 Hz, respectively, in this study. Zircon 91,500 and glass NIST610 were used as external standards for U-Pb dating and trace element calibration, respectively. Each analysis incorporated a background acquisition of approximately 20–30 s followed by 50 s of data acquisition from the sample. An Excel-based software ICPMSDataCal was used to perform off-line selection and integration of background and analyzed signals, time-drift correction and quantitative calibration for trace element analysis and U-Pb dating (Liu et al., 2008, 2010). Concordia

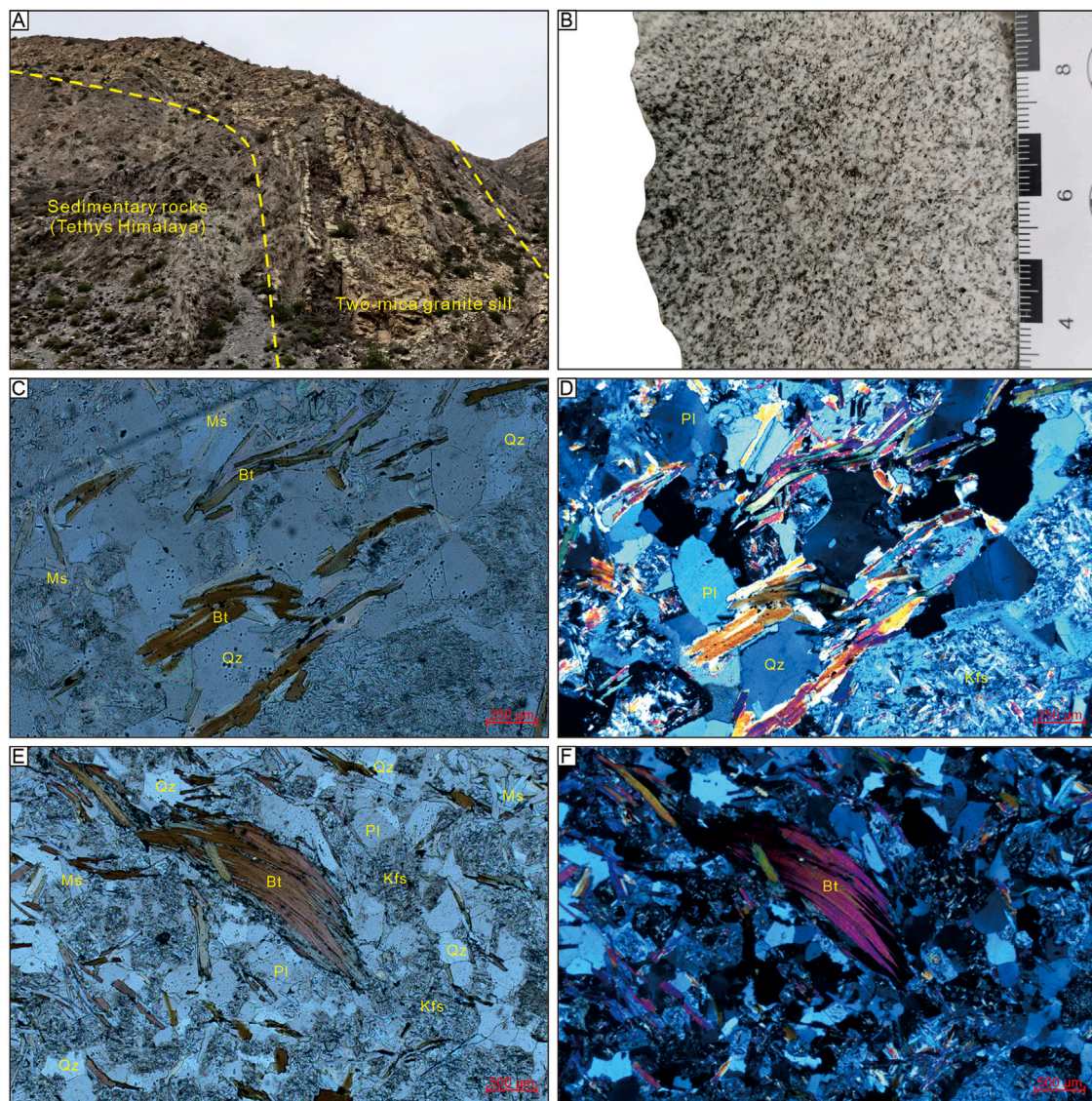


**FIGURE 3**

(A) Field photograph, (B) hand specimen photograph, and (C–F) representative photomicrographs of the Liemai two-mica granite [(C) and (E), plane-polarized light; (D) and (F), crossed-polarized light]. Bt, biotite; Kfs, K-feldspar; Pl, plagioclase; Qz, quartz.

diagrams and weighted mean calculations were made using Isoplot/Ex\_ver3 (Ludwig, 2003).

Experiments of *in situ* Hf isotope ratio analysis were conducted using a Neptune Plus MC-ICP-MS (Thermo Fisher Scientific, Germany) in combination with a Geolas HD excimer ArF laser ablation system (Coherent, Göttingen, Germany) that was hosted at the Wuhan Sample Solution Analytical Technology Co., Ltd. All the Hf analyses were done on the same or equivalent spots as those for U-Pb laser ablation analyses. A stationary laser ablation spot with a beam diameter of 32  $\mu\text{m}$  was used for the analyses. Detailed operating conditions for the laser ablation system and the MC-ICP-MS instrument and analytical method

were described in Hu et al. (2012). The major limitation to accurate *in situ* zircon Hf isotope determination by LA-MC-ICP-MS is the very large isobaric interference from  $^{176}\text{Yb}$  and, to a much lesser extent  $^{176}\text{Lu}$  on  $^{176}\text{Hf}$ . It has been shown that the mass fractionation of Yb ( $\beta_{\text{Yb}}$ ) isn't constant over time and that the  $\beta_{\text{Yb}}$  that is obtained from the introduction of solutions is unsuitable for *in situ* zircon measurements (Woodhead et al., 2004). The under- or over-estimation of the  $\beta_{\text{Yb}}$  value would undoubtedly affect the accurate correction of  $^{176}\text{Yb}$  and thus the determined  $^{176}\text{Hf}/^{177}\text{Hf}$  ratio. We applied the directly obtained  $\beta_{\text{Yb}}$  value from the zircon sample itself in real-time in this study. The  $^{179}\text{Hf}/^{177}\text{Hf}$  and  $^{173}\text{Yb}/^{171}\text{Yb}$  ratios were used to calculate the

mass bias of Hf ( $\beta_{\text{Hf}}$ ) and Yb ( $\beta_{\text{Yb}}$ ), which were normalized to  $^{179}\text{Hf}/^{177}\text{Hf} = 0.7325$  and  $^{173}\text{Yb}/^{171}\text{Yb} = 1.132685$  (Fisher et al., 2014) using an exponential correction for mass bias. Interference of  $^{176}\text{Yb}$  on  $^{176}\text{Hf}$  was corrected by measuring the interference-free  $^{173}\text{Yb}$  isotope and using  $^{176}\text{Yb}/^{173}\text{Yb} = 0.79639$  (Fisher et al., 2014) to calculate  $^{176}\text{Yb}/^{177}\text{Hf}$ . Similarly, the relatively minor interference of  $^{176}\text{Lu}$  on  $^{176}\text{Hf}$  was corrected by measuring the intensity of the interference-free  $^{175}\text{Lu}$  isotope and using the recommended  $^{176}\text{Lu}/^{175}\text{Lu} = 0.02656$  (Blichert-Toft et al., 1997) to calculate  $^{176}\text{Lu}/^{177}\text{Hf}$ . We used the mass bias of Yb ( $\beta_{\text{Yb}}$ ) to calculate the mass fractionation of Lu because of their similar physicochemical properties. Off-line selection and integration of analyte signals, and mass bias calibrations were performed using ICPMSDataCal (Ludwig, 2003).

### 3.2 Monazite U-Th-Pb dating

Similar to zircons, monazite separation and sample processing were conducted at the Langfang Regional Geological Survey. Transmitted, reflected, and BSE images, which were obtained at the Wuhan Sample Solution Analytical Technology Co., Ltd (Hubei Province, China), were used to determine internal features of monazite grains. Twenty-five eu- to subhedral monazite grains without obvious inclusions were selected for *in situ* LA-ICP-MS isotopic and compositional analyses. U-Pb dating of monazite was conducted by LA-ICP-MS at the Wuhan Sample Solution Analytical Technology Co., Ltd. Laser sampling was performed using a GeolasPro laser ablation system that consists of a COMPexPro 102 ArF excimer laser (wavelength of 193 nm) and a MicroLas optical system. An Agilent 7700e ICP-MS instrument was used to acquire ion-signal intensities. Helium was applied as a carrier gas. Argon was used as the make-up gas and mixed with the carrier gas *via* a T-connector before entering the ICP. A “wire” signal smoothing device is included in this laser ablation system, by which smooth signals are produced even at very low laser repetition rates down to 1 Hz (Hu et al., 2015). It is very useful for *in-situ* U-Pb dating of high-U mineral (Zong et al., 2015). The spot size and frequency of the laser were set to 16  $\mu\text{m}$  and 2 Hz, respectively. The laser energy was set to 80 mJ. Monazite standard 44069 and glass NIST610 were used as external standards for U-Pb dating and trace element calibration, respectively. Each analysis incorporated a background acquisition of approximately 20–30 s followed by 50 s of data acquisition from the sample. An Excel-based software ICPMSDataCal was used to perform off-line selection and integration of background and analyzed signals, time-drift correction and quantitative calibration for trace element analysis and U-Pb dating (Liu et al., 2008, 2010). Concordia diagrams and weighted mean calculations were made using Isoplot/Ex\_ver3 (Ludwig, 2003).

### 3.3 Whole-rock major and trace elements

Major and trace element contents were analyzed at the Beijing Research Institute of Uranium Geology. The fresh rock samples were chipped and powdered to a mesh size of  $\sim 200$  using a tungsten carbide ball mill. The details of the analytical procedures are described by Gao et al. (2003). Major oxide analyses were conducted using a PANalytical Axios MAX X-ray Fluorescence Spectrometer with an analytical uncertainty of  $<5\%$ . The trace element concentrations were analyzed using a Perkin-Elmer NexIon 300D ICPMS with an analytical precision of  $<1\%$  for elements with concentrations  $>200$  ppm and  $1\%–3\%$  for elements with concentrations  $<200$  ppm.

### 3.4 Whole-rock Sr-Nd-Pb isotopes

Whole-rock Sr-Nd-Pb isotopes were analyzed at the Beijing Research Institute of Uranium Geology. Approximately 200 mg of each sample powder was dissolved in an HF + HNO<sub>3</sub> acid mixture for 48 h in a Teflon beaker. All samples were prepared in duplicate. The digests were dried, dissolved in hydrochloric acid and heated in closed vials at 160 C for 1 h, and evaporated to dryness. The Sr and Nd were separated and purified by conventional cation-exchange techniques. The initial  $^{87}\text{Sr}/^{86}\text{Sr}$  ratios and  $\epsilon_{\text{Nd}}(t)$  values at the time of crystallization were calculated from the weighted mean zircon U-Pb age and the Rb, Sr, Sm and Nd contents. When calculating the  $\epsilon_{\text{Nd}}(t)$  values, we assumed the model composition of a chondritic uniform reservoir at the estimated age. The  $T_{\text{DM1}}$  and  $T_{\text{DM2}}$  values are the estimated ages of extraction from the depleted mantle according to the one-stage and two-stage crustal pre-histories, respectively, as assumed by Depaolo (1988) and Depaolo et al. (1991). The precision of the calculated initial  $^{87}\text{Sr}/^{86}\text{Sr}$  values is limited by the errors in the parent/daughter ratios calculated from the geochemical data. Nevertheless, in most cases, errors as high as  $\pm 10\%$  in the Rb/Sr ratio introduce uncertainties below 0.0001 in the initial  $^{87}\text{Sr}/^{86}\text{Sr}$  values (Dolgoplova et al., 2013), and a 10% error in the Nd isotopes results in an uncertainty of about 0.4–0.7 in the  $\epsilon_{\text{Nd}}(t)$  values. The measured Pb isotopic ratios were corrected for the instrumental mass fractionation of 0.1 amu<sup>-1</sup> by referencing to repeat analyses of the standard NBS-981.

## 4 Results

### 4.1 Zircon U-Pb ages and Hf isotopes

U-Pb dating and trace elements results for zircons of the Liemai two-mica granite are shown in appendix (Supplementary Table S1). Cathodoluminescence (CL) images of representative zircon grains from the Liemai two-mica granite are shown in

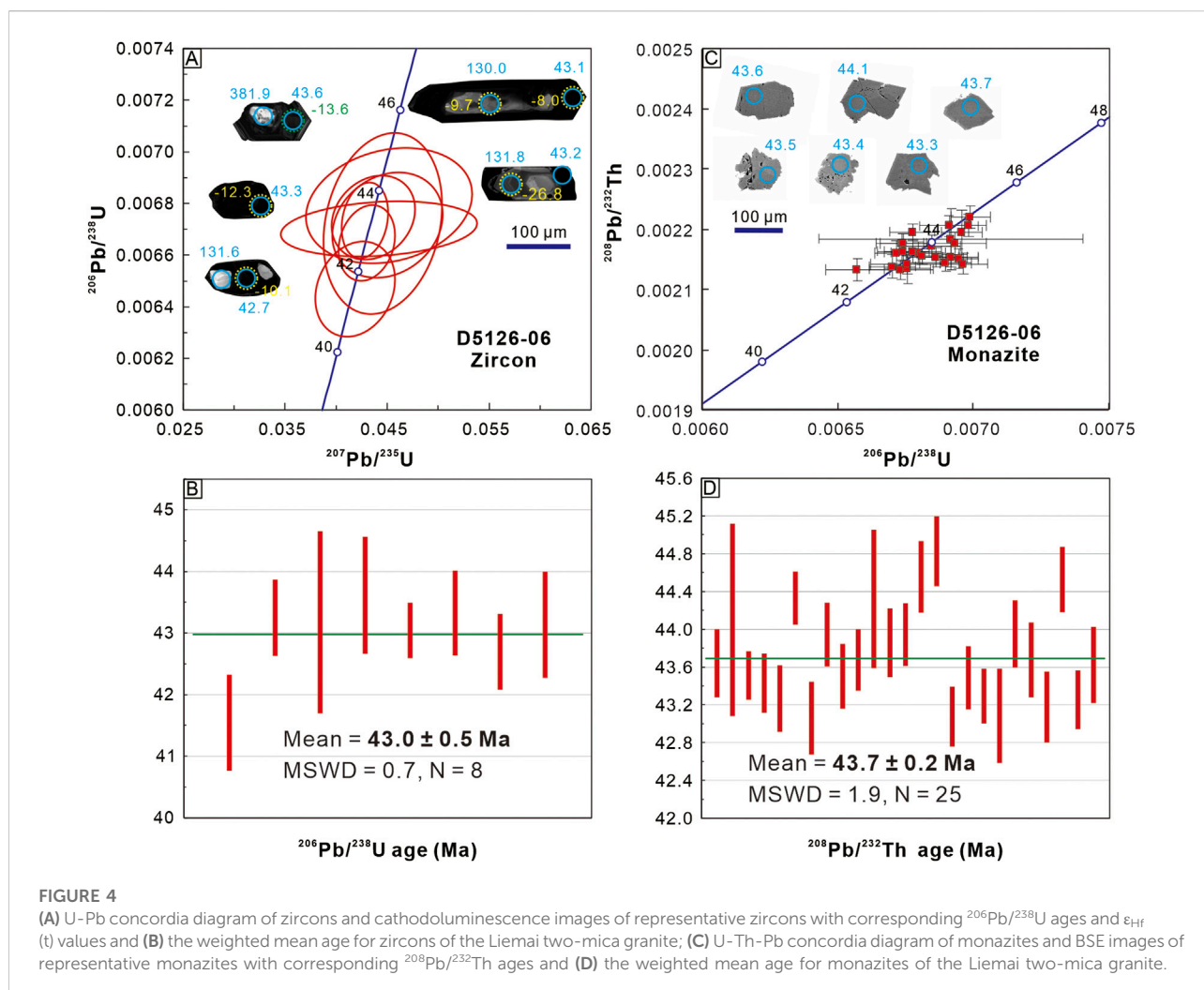


**Figure 4A.** Eu- to subhedral zircon crystals are long prismatic (80–200  $\mu\text{m}$ ), with aspect ratios of 2:1 to 5:1. Most zircon grains exhibit core-(mantle)-rim structure with gray subhedral to anhedral cores and dark rims (**Figure 4A**). The inherited cores normally show obvious oscillatory growth zoning (**Figure 4A**), suggesting magmatic origin (**Wu and Zheng, 2004**). In contrast, some rims display weak but visible oscillatory overgrowth zoning indicating magmatic origin, some others show no oscillatory overgrowth zoning and are homogeneous suggesting metamorphosed origin (**Figure 4A**; **Wu and Zheng, 2004**; **Hoskin, 2005**). Detailed description of zircon structure and analytical position are shown in appendix (**Supplementary Table S1**). Twenty-three analyses (with a concordance of >90%) yield  $^{206}\text{Pb}/^{238}\text{U}$  ages ranging from 41.6 to 1721.5 Ma. Fifteen analyses on inhibited cores yield  $^{206}\text{Pb}/^{238}\text{U}$  ages ranging from 130.0 to 1721.5 Ma. Eight analyses on dark rims or zircons without inherited cores yield  $^{206}\text{Pb}/^{238}\text{U}$  ages ranging from 41.6 to 43.6 Ma with a weighted Eocene mean age of  $43.0 \pm 0.5$  Ma (MSWD = 0.7) (**Figure 4B**).

Thirteen spots were also analyzed for Lu-Hf isotopes. The analytical results are listed in appendix (**Supplementary Table S2**). The analyzed zircon grains have  $^{176}\text{Lu}/^{177}\text{Hf}$  ratios of 0.000018–0.003409 and  $^{176}\text{Hf}/^{177}\text{Hf}$  ratios of 0.281963–0.282520. Except for one analysis (D5126-06-24), zircon crystals display  $^{176}\text{Lu}/^{177}\text{Hf}$  ratios <0.002, indicating extremely low accumulations of the radioactive Hf isotope after crystallization (**Wu et al., 2007**). Seven analyses on juvenile zircon rims yield calculated  $\epsilon_{\text{Hf}}$  (t) ( $t = 43$  Ma) values of –14.3 to –8.0 (average of –11.1) with two stage Hf model ages ( $T_{\text{DM}2}$ ) of 1,027–1,256 Ma.

## 4.2 Monazite U-Th-Pb ages

The monazite U-Th-Pb dating and trace elements results for the Liemai two-mica granite are listed in appendix (**Supplementary Table S3**). The BSE images of representative monazites are shown in **Figure 4C**. All monazite grains are grey in BSE images, and most of them are homogeneous, although some grains show zoning

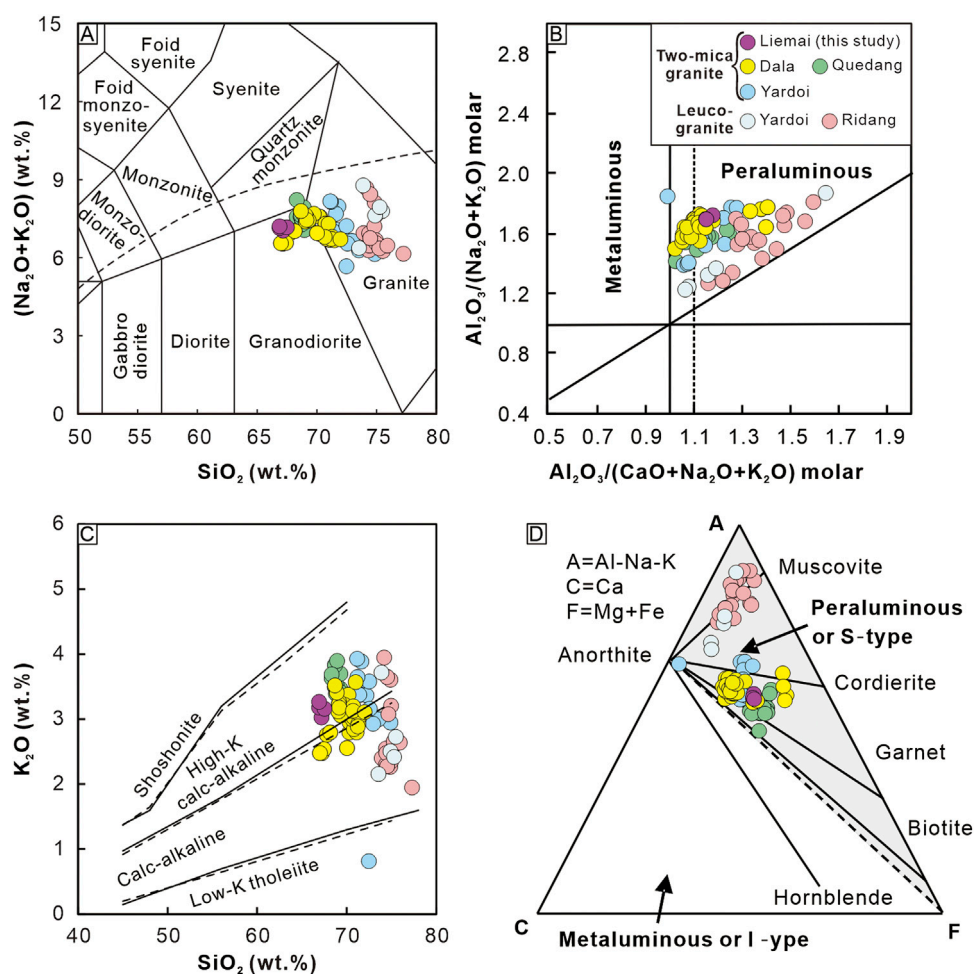


FIGURE 5

(A)  $\text{SiO}_2$  vs.  $\text{K}_2\text{O} + \text{Na}_2\text{O}$  (Middlemost, 1994), (B)  $\text{A}/\text{CNK}$  vs.  $\text{A}/\text{NK}$  (Maniar and Piccoli, 1989), (C)  $\text{SiO}_2$  vs.  $\text{K}_2\text{O}$  (Rickwood, 1989), and (D) A-C-F (Chappell and White, 1992) diagrams for the Liemai two-mica granite. Data source: Quedang two-mica granites are from Zeng et al. (2011) and Hou et al. (2012); Dala two-mica granites are from Zeng et al. (2011, 2015), Hou et al. (2012) and Dai et al. (2020a); Yardo two-mica granites are from Zeng et al. (2011, 2015); Yardo leucogranites are from Zeng et al. (2015); Ridang leucogranites (subvolcanic rocks) are from Hu et al. (2011b) and Zeng et al. (2015).

(Figure 4C). The monazites in the Liemai two-mica granite have high contents of Th (37,794–113,394 ppm) and U (1,663–9,254 ppm), and relatively low Pb contents (83–245 ppm). The  $^{207}\text{Pb}/^{235}\text{U}$  ages of these monazites are scattered, ranging from 59.3 to 251.9 Ma. In contrast, the  $^{206}\text{Pb}/^{238}\text{U}$  ages (42.2–44.9 Ma) and  $^{208}\text{Pb}/^{232}\text{Th}$  ages (43.1–44.8 Ma with a weighted Eocene mean age of  $43.7 \pm 0.2$  Ma,  $N=25$ ,  $\text{MSWD} = 0.7$ ; Figure 4D) are very concentrated. In addition, the  $^{206}\text{Pb}/^{238}\text{U}$  ages and  $^{208}\text{Pb}/^{232}\text{Th}$  ages are very concordant with each other (Figure 4D).

### 4.3 Whole-rock major and trace elements

The whole-rock major and trace element data for the Liemai two-mica granite are listed in appendix (Supplementary Table

S4). Samples are characterized by high contents of  $\text{SiO}_2$  (66.88–67.48 wt.%),  $\text{Al}_2\text{O}_3$  (16.24–16.44 wt.%),  $\text{Na}_2\text{O}$  (3.72–3.83 wt.%) and  $\text{K}_2\text{O}$  (3.03–3.27 wt.%), and relatively low contents of  $\text{CaO}$  (2.42–2.52 wt.%), total iron ( $\text{TFeO} = 2.06$ – $2.11$  wt.%  $\text{TiO}_2$  (0.31–0.33 wt.%),  $\text{MnO}$  (0.03–0.04 wt.%),  $\text{MgO}$  (1.24–1.29 wt.%), and  $\text{P}_2\text{O}_5$  (0.13–0.14 wt.%) with relatively high  $\text{Na}_2\text{O}/\text{K}_2\text{O}$  mass ratios (1.14–1.25) and  $\text{Mg\#}$  [ $\text{Mg\#} = \text{MgO} \times 100 / (\text{MgO} + \text{FeO}^{\text{T}})$  (molar ratio)] values (51.75–52.20) (Supplementary Table S4). The total alkali contents ( $\text{K}_2\text{O} + \text{Na}_2\text{O}$ ) range from 6.82 to 6.99 wt.%, indicative of sub-alkaline series in the total alkalis vs. silica (TAS) diagram (Figure 5A; Middlemost, 1994). The  $\text{A}/\text{CNK}$  values [ $\text{A}/\text{CNK} = \text{Al}_2\text{O}_3 / (\text{CaO} + \text{Na}_2\text{O} + \text{K}_2\text{O})$  (molar ratio)] vary from 1.15 to 1.17, whereas the  $\text{A}/\text{NK}$  values [ $\text{A}/\text{NK} = \text{Al}_2\text{O}_3 / (\text{Na}_2\text{O} + \text{K}_2\text{O})$  (molar ratio)] range from 1.69 to 1.72, indicating peraluminous features

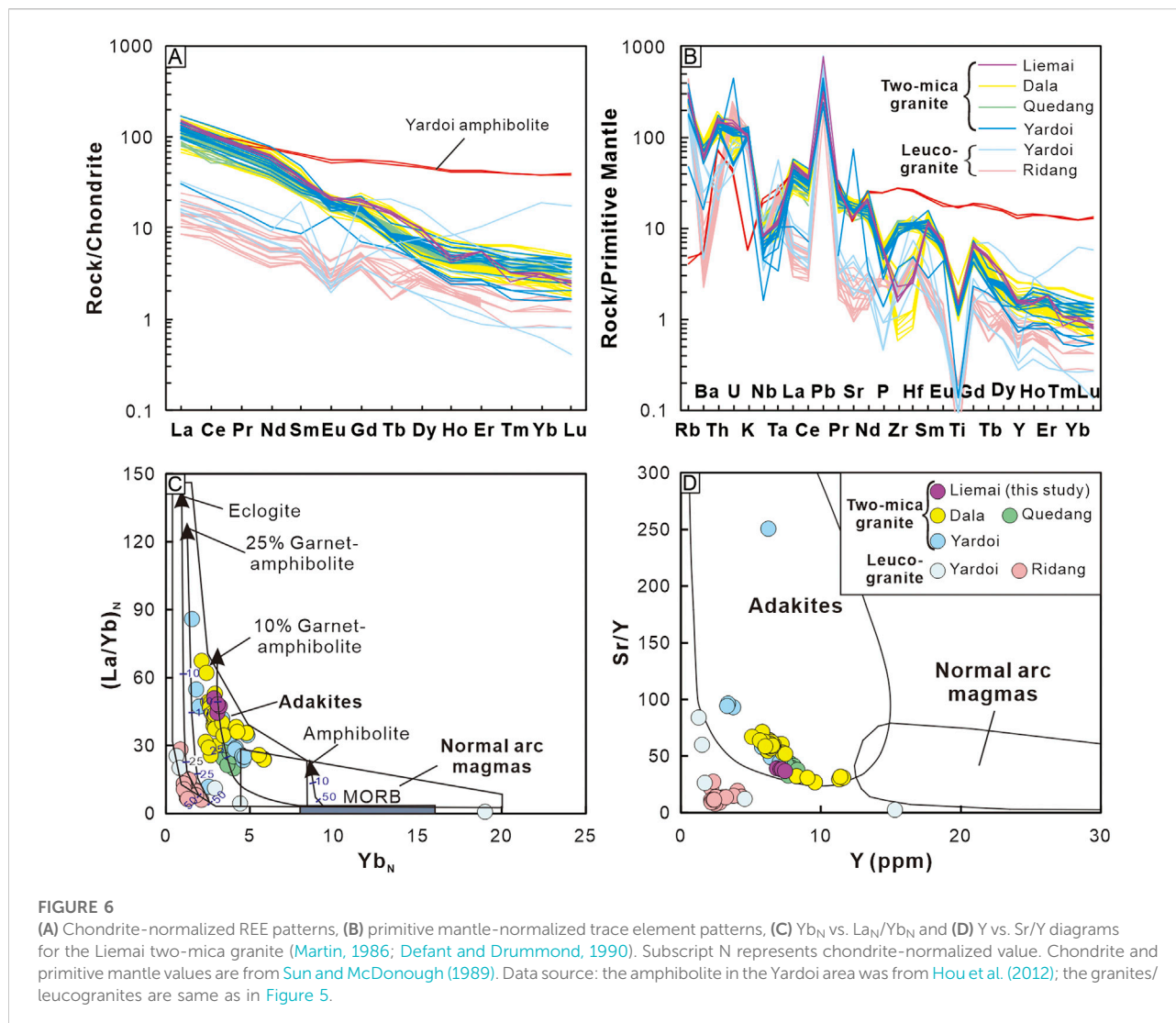


(Figure 5B; Maniar and Piccoli, 1989). On the  $K_2O$  vs.  $SiO_2$  diagram, the samples show high-K calc-alkaline characteristics (Figure 5C; Peccerillo and Taylor, 1976). On the A-F-C diagram, the Liemai two-mica granite samples plot in the peraluminous granitoid-type field (Figure 5D; Chappell and White, 1992).

The Liemai two-mica granite is characterized by LREE (light rare Earth element) enrichment and HREE (heavy rare Earth element) depletion with high LREE/HREE ratios (16.0–16.7; Supplementary Table S4), suggesting significant differentiation of LREE from HREE. This is in accordance with the right-leaning chondrite-normalized REE patterns (Figure 6A). The Liemai two-mica granite displays an indistinctive negative Eu anomaly ( $Eu/Eu^* = 0.7\sim 0.8$ ; Supplementary Table S4; Figure 6A). The rock is enriched in LILE (large ion lithophile element) such as Rb and K and depleted in HFSE (high field strength element) such as Nb, Ta, Zr, Hf, and Ti (Figure 6B). Importantly, the Liemai two-mica granite has low concentrations of Y (6.9~7.4 ppm) and Yb

(~0.5 ppm) and relatively high concentrations of Sr (269~278 ppm) and La (32.3~36.0 ppm) with high Sr/Y (36.8~39.2) and  $(La/Yb)_N$  (44.5~50.9) ratios (subscript N represents chondrite-normalized value based on Sun and McDonough, 1989), showing adakitic features (Figures 6C, D; Martin, 1986; Defant and Drummond, 1990).

#### 4.4 Whole-rock Sr-Nd-Pb isotopes

The whole-rock Sr-Nd-Pb isotopic compositions of the Liemai two-mica granite are listed in appendix (Supplementary Table S5). The samples have low  $(^{87}Sr/^{86}Sr)_i$  ratios (0.718414–0.718423) and negative  $\epsilon_{Nd}(t)$  values (–14.7 to –13.9), with  $T_{DM2}$  ranging from 1,803 to 1,852 Ma. The  $(^{206}Pb/^{204}Pb)_i$ ,  $(^{207}Pb/^{204}Pb)_i$ , and  $(^{208}Pb/^{204}Pb)_i$  values are 18.781–18.791, 15.687–15.695 and 39.214–39.236, respectively. All initial values are calculated for 43 Ma.

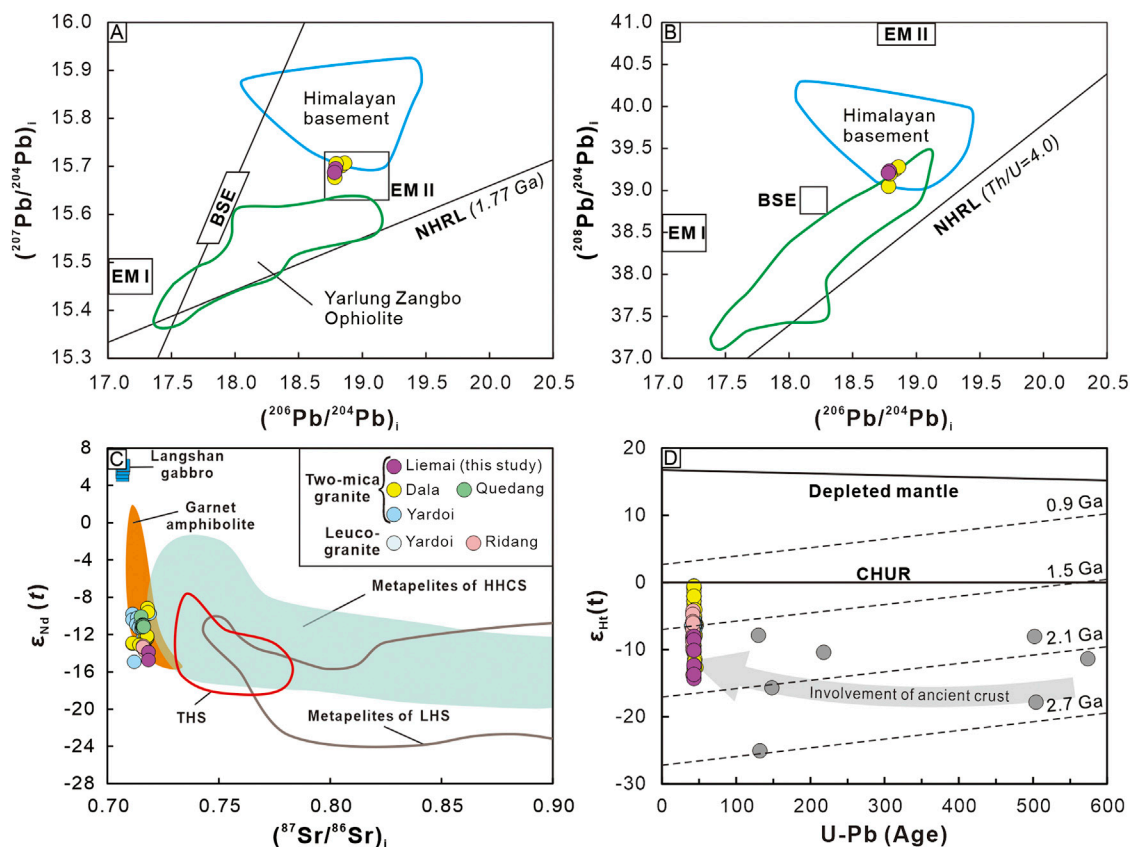


FIGURE 7

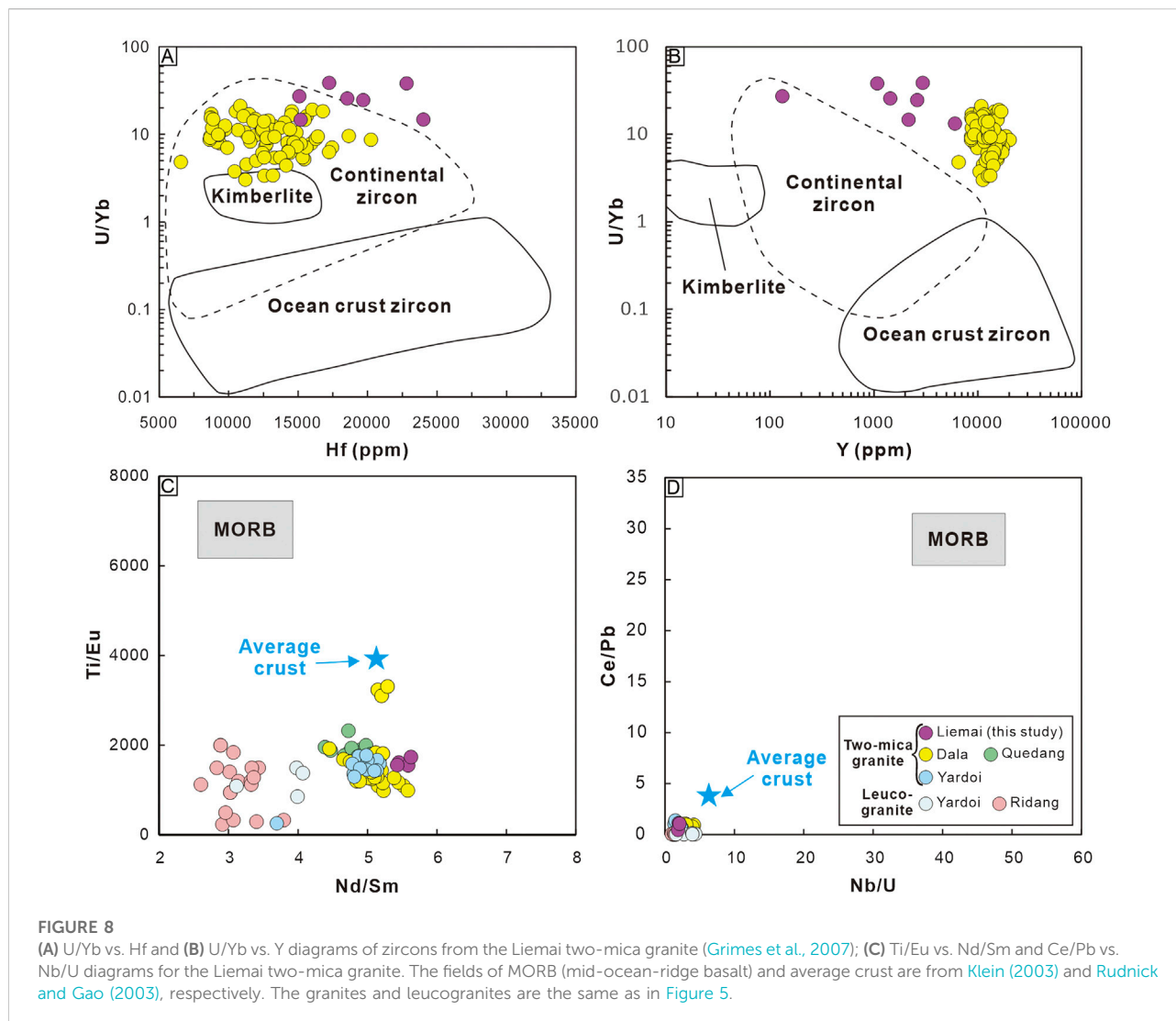
(A)  $(^{207}\text{Pb}/^{204}\text{Pb})_i$  vs.  $(^{206}\text{Pb}/^{204}\text{Pb})_i$ , (B)  $(^{208}\text{Pb}/^{204}\text{Pb})_i$  vs.  $(^{206}\text{Pb}/^{204}\text{Pb})_i$ , (C)  $\epsilon_{\text{Nd}}(t)$  vs.  $(^{87}\text{Sr}/^{86}\text{Sr})_i$ , and (D)  $\epsilon_{\text{Hf}}(t)$  vs. U-Pb age diagrams for the Liemai two-mica granite. Data source: the Himalayan basement is from Vidal et al. (1982) and Harrison et al. (1999); the Yarlung Zangbo Ophiolite are from Xu and Castillo (2004), Zhang et al. (2005) and Niu et al. (2006); the Bulk Silicate Earth (BSE) and enriched mantle components (EM I and EM II) are from Zindler and Hart (1986); the Langshan gabbro is from Ji et al. (2016); the garnet amphibolite is from Zeng et al. (2011); the metapelites of HHCS are from Inger and Harris (1993), Yang and Jin (2001), Richards et al. (2005) and Zeng et al. (2009, 2012); the LHS and THS are from Richards et al. (2005); the granites/leucogranites are the same as in Figure 5. Northern Hemisphere Reference Line (NHRL):  $^{207}\text{Pb}/^{204}\text{Pb} = 0.1084 \times ^{206}\text{Pb}/^{204}\text{Pb} + 13.491$ ;  $^{208}\text{Pb}/^{204}\text{Pb} = 1.209 \times ^{206}\text{Pb}/^{204}\text{Pb} + 15.627$ . All initial isotopic ratios are corrected to  $t = 43$  Ma.

## 5 Discussion

### 5.1 Formation age for the Liemai two-mica granite

As mentioned above, the juvenile zircon rims with oscillatory zoning in the Liemai two-mica granite are magmatic while those without oscillatory zoning are of metamorphosed origin. Interestingly, these rims have undistinguishable  $^{206}\text{Pb}/^{238}\text{U}$  ages (Supplementary Table S1). This indicates that metamorphism and partial melting of the source rock for the Liemai two-mica granite were possibly coeval. This phenomenon has been recorded in the Yardoi dome (Zeng et al., 2011). Therefore, the weighted  $^{206}\text{Pb}/^{238}\text{U}$  age of juvenile zircon rims ( $43.0 \pm 0.5$  Ma) can be interpreted as the timing of partial melting of the source rock and the formation age of the Liemai two-mica granite.

Monazite incorporates a significant amount of  $^{230}\text{Th}$  into its crystal structure during crystallization, which will lead to generation of “excess”  $^{206}\text{Pb}$  and result in disequilibrium in the  $^{238}\text{U} \rightarrow ^{206}\text{Pb}$  decay. In juvenile monazite (Cenozoic), the “excess”  $^{206}\text{Pb}$  will lead to apparent  $^{206}\text{Pb}/^{238}\text{U}$  ages that are older than measured  $^{207}\text{Pb}/^{235}\text{U}$  and  $^{208}\text{Pb}/^{232}\text{Th}$  ages. Besides, due to their young age, such monazites normally contain low contributions of radiogenic  $^{207}\text{Pb}$ , which will result in  $^{207}\text{Pb}/^{235}\text{U}$  ages that are less precise than  $^{206}\text{Pb}/^{238}\text{U}$  and  $^{208}\text{Pb}/^{232}\text{Th}$  ages. In contrast, owing to high contents of  $^{232}\text{Th}$  (wt.% levels) and therefore significant  $^{208}\text{Pb}$  in monazite,  $^{208}\text{Pb}/^{232}\text{Th}$  ages can be taken as the best estimate of the monazite crystallization age (Cottle et al., 2015). Therefore, the weighted  $^{208}\text{Pb}/^{232}\text{Th}$  age ( $43.7 \pm 0.2$  Ma) are interpreted as crystallization age of monazites in the Liemai two-mica granite. Owing to relatively low closure temperature and high sensitivity, inherited monazites are very rare even in low-temperature granites (Parrish, 1990). Thus, the weighted  $^{208}\text{Pb}/^{232}\text{Th}$  age ( $43.7 \pm 0.2$  Ma) of



monazites in the Liemai two-mica granite can be interpreted as formation age of the rock.

In summary, the weighted  $^{206}\text{Pb}/^{238}\text{U}$  age of juvenile zircons are consistent with the weighted  $^{208}\text{Pb}/^{232}\text{Th}$  age of monazites within errors, indicating that the Liemai two-mica granite was generated at  $\sim 43.5$  Ma, coeval to two-mica granites in Yardoi, Dala, Quedang (Figure 2).

## 5.2 Petrogenesis of the Early Eocene granites in the Yardoi area

### 5.2.1 Petrogenesis of the Liemai two-mica granite

In despite of strong peraluminous features, the high Sr/Y (36.8–39.2) and  $(\text{La}/\text{Yb})_N$  (44.5–50.9) ratios of the Liemai

two-mica are indicative of its adakitic attribution (Figures 6C, D; Martin, 1986; Defant and Drummond, 1990). Several models have been proposed for the genesis of adakitic rocks since Defant and Drummond (1990) defined this rock type based on its geochemical features: 1) partial melting of subducted oceanic crust (Defant and Drummond, 1990; Zhu et al., 2009b; Dai et al., 2018); 2) crustal assimilation and fractional crystallization (AFC) processes from parental basaltic magmas (Castillo et al., 1999; Macpherson et al., 2006; Wang et al., 2020); 3) mixing of felsic and basaltic magmas (Streck et al., 2007; Chu et al., 2020); 4) partial melting of thickened lower crust (Long et al., 2015; Yang et al., 2016b); 5) partial melting of delaminated lower crust (Xu et al., 2002; Dai et al., 2020b) and 6) partial melting of subducted continental crust (Jiang et al., 2011; Lai and Qin, 2013). These possibilities will be discussed below.

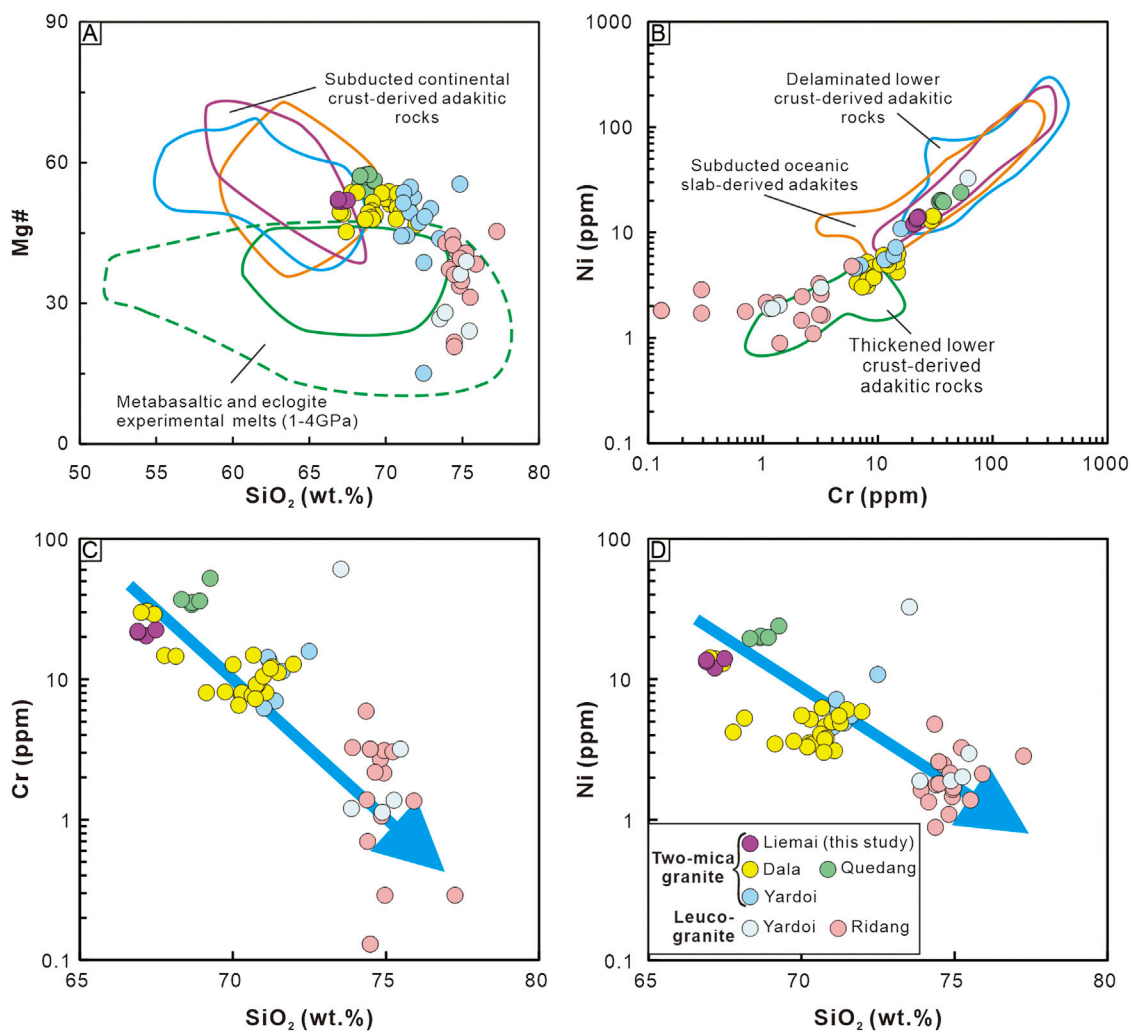


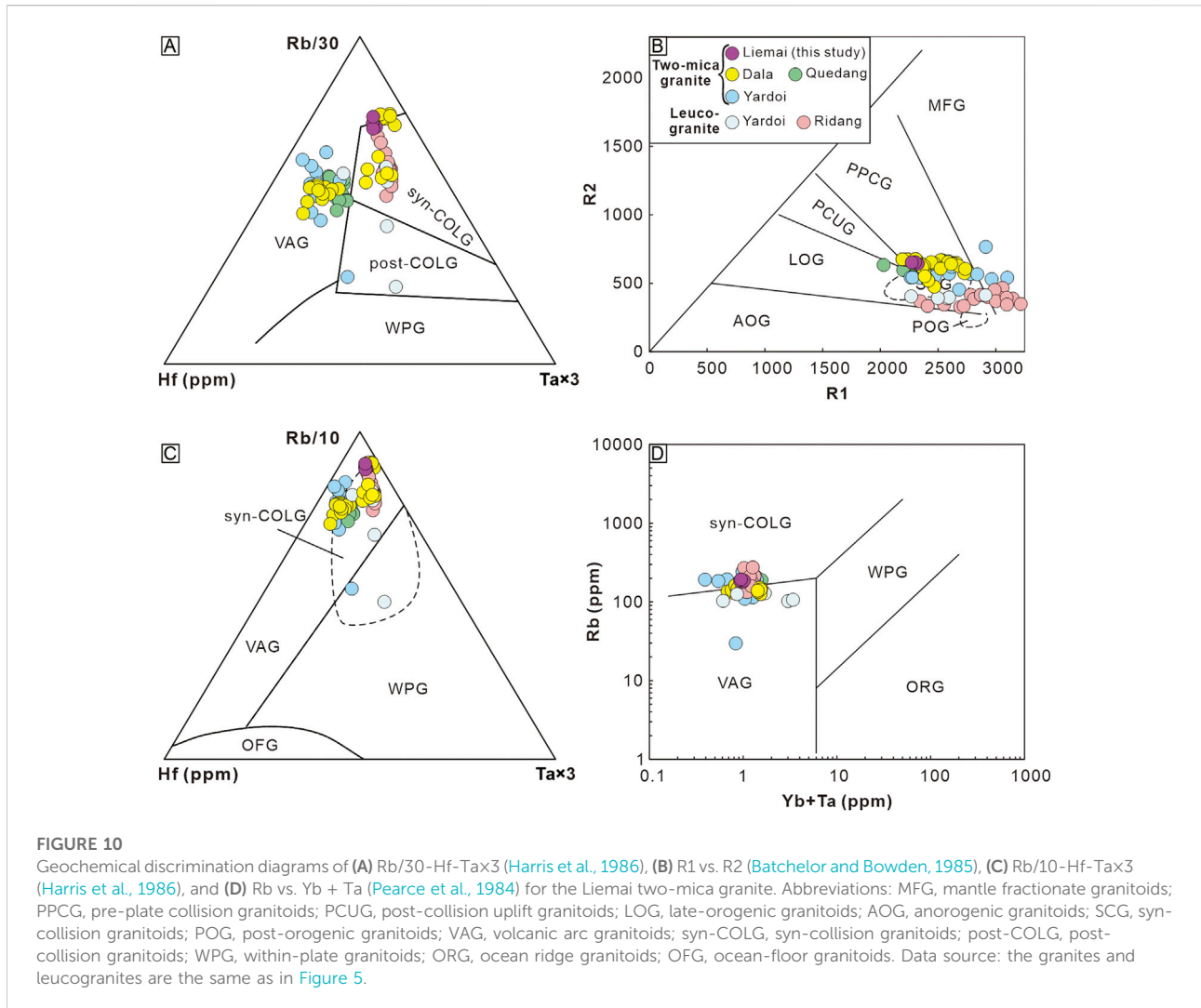
FIGURE 9

(A) Mg# vs.  $\text{SiO}_2$ , (B) Ni vs. Cr, (C) Cr vs.  $\text{SiO}_2$  and (D) Ni vs.  $\text{SiO}_2$  diagrams for the Liemai two-mica granite. Data source: metabasaltic and eclogite experimental melts (1–4 GPa) are from Rapp et al. (1999, 2002); subducted oceanic slab-derived adakites are from Zhu et al. (2009b), Zhang et al. (2010), Jiang et al. (2012), Ma et al. (2013) and Dai et al. (2018); subducted continental crust-derived adakitic rocks are from Jiang et al. (2011) and Lai and Qin (2013); thickened lower crust-derived adakitic rocks are from Ma et al. (2014), Long et al. (2015) and Yang et al. (2016b); delaminated lower crust-derived adakitic rocks are from Xu et al. (2002, 2006), Gao et al. (2004), Wang et al. (2006, 2014), Karsli et al. (2010) and Chen et al. (2013); other granites and leucogranites are the same as in Figure 5.

The Pb isotopes of the Liemai two-mica granite are similar to those of the Himalayan basement but differ from those of the Yarlung Zangbo ophiolite (Figures 7A, B), precluding the subducted oceanic crust and supporting the Himalayan crust as a possible magma source. The distinct Sr-Nd isotopes of the Liemai two-mica granite from those of the coeval Langshan gabbro (Figure 7C; Ji et al., 2016) and absent of dark enclaves (Figure 3B) are inconsistent with hypotheses of fractional crystallization (Macpherson et al., 2006; Wang et al., 2020) and mixing of felsic and basaltic magmas (Chu et al., 2020), respectively. Instead, enrichment of Th, U and Pb, and large

negative zircon  $\varepsilon_{\text{Hf}}(t)$  values (–14.3 to –8.0) with old  $T_{\text{DM}2}$  (1,027–1,256 Ma) of the Liemai two-mica suggest an ancient crustal source. In addition, the Liemai two-mica granite shows notable continental crust affinities on the U/Yb vs. Hf and U/Yb vs. Y diagrams of zircons and whole-rock Ti/Eu vs. Nd/Sm and Ce/Pb vs. Nb/U diagrams (Figure 8).

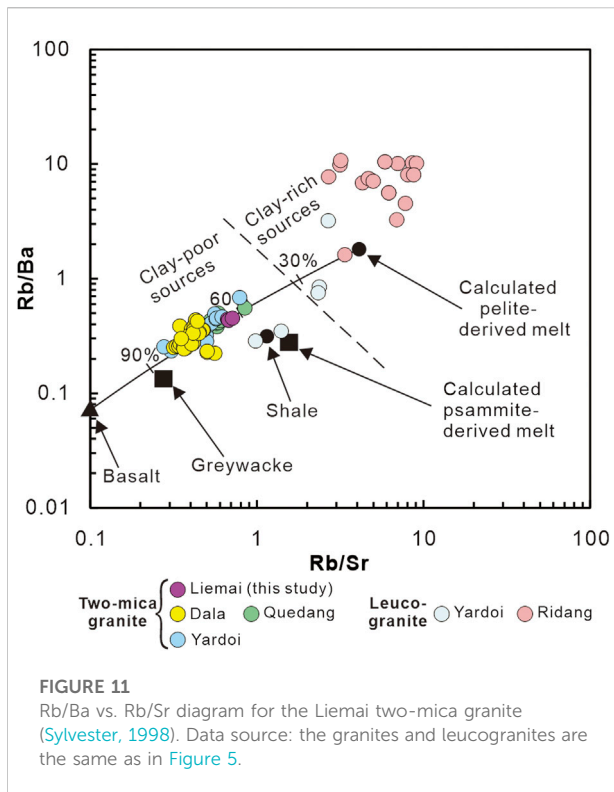
Commonly, crust-derived melts display low concentrations of MgO, Mg# values and compatible elements (such as Cr and Ni) (Ma et al., 2014; Long et al., 2015; Yang et al., 2016b). However, delaminated thickened lower crust- and subducted continental crust-derived melts typically shows elevated MgO,



Mg# values and compatible element concentrations owing to interaction with overlying mantle peridotite during ascent (Xu et al., 2002; Jiang et al., 2011; Lai and Qin, 2013; Dai et al., 2020b). The Liemai two-mica granite show a little bit higher concentrations of Mg# (52 on average) and Cr (21.7 ppm on average) and Ni (13.4 ppm on average) than typical thickened lower crust-derived magmas and experimental products of partial melting of metabasalt and eclogite (Mg# < 45; Cr < 15 ppm; Ni < 5 ppm; Figures 9A, B), seemingly suggesting an origin related to subduction of oceanic or continental crust or delamination of lower continental crust. Subduction origin can be easily excluded since subduction-related magmas occur in active continental margin while the Himalayan terrane was a passive continental margin of the Neo-Tethys Ocean (Pan et al., 2012; Zhu et al., 2015). In addition, delamination of lower crust typically occurs at an extensional tectonic background typically during late stage of collision (Hou et al., 2004; Wang et al., 2006,

2014). Although a temporary extension tectonic regime could be possible owing to continental rebound owing to pull force loss resulted from slab detachment of the Noe-Tethys lithosphere. In the Paleogene, owing to intensive collision between India and Eurasia, compressional and contractional tectonic regime dominated the Himalaya orogen (Hou et al., 2006a; 2006b). This is consistent with syn-collisional geochemical signatures of the Liemai two-mica granites (Figure 10). Thus, partial melting of a thickened lower crust is a more preferable interpretation for genesis of the Liemai two-mica granite. Relatively higher contents of Mg#, Ni and Cr could probably be caused by relatively high contents of biotite (Figures 9B–F, 3B–F).

Zircon U-Pb and monazite U-Th-Pb dating results in this study imply that the metamorphism and anatexis of the source rock of the Liemai two-mica granite occurred at ~43.5 Ma. This is coincidence with the contemporaneous metamorphism and partial melting of garnet amphibolite (43.5 ± 1.3 Ma; Zeng



et al., 2011) in the Yardoi dome. In addition, Sr-Nd isotopes of the Liemai two-mica granite are similar to those of the garnet amphibolite (Figure 7C). This indicates that the garnet amphibolite would be the major source rock for the Liemai two-mica granite. Relatively high Rr/Sr and Rb/Ba values indicate that minor metapelites were also probably present in the source region (Figure 11), although the abnormally high Rr/Sr and Rb/Ba ratios could have probably been caused by extreme magma evolution.

In summary, the Liemai two-mica granite is a product of partial melting of thickened lower crust consisting mainly of amphibolite with minor metapelites. This, in turn, manifests that the Early Eocene adakitic rocks in the Yardoi area share a same origin, which is supported by their similar formation ages (Figure 2), geochemical (Figures 5, 6, 8–11) and isotopic (Figure 7) compositions.

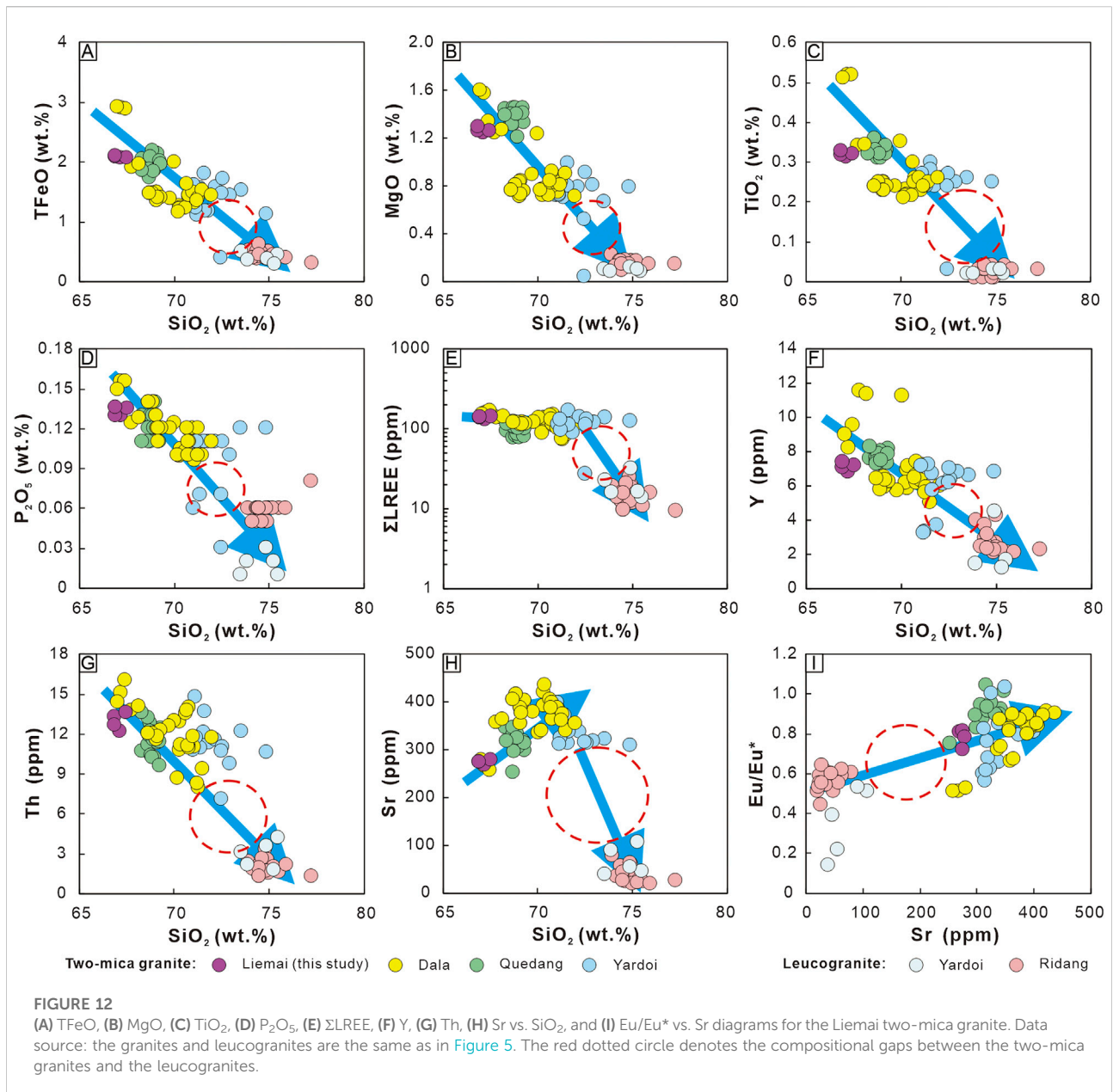
### 5.2.2 Genetic relationship between the high-Mg# granites and low-Mg# granites

Besides two-mica granite, there are also some other types of coeval granites exposed in the Yardoi area, including subvolcanic porphyritic leucogranite and leucogranite. These adjacent granites have similar formation ages (Figure 2) and Sr–Nd–Hf isotope systematics (Figure 7), suggesting an identical origin. Nevertheless, discernible differences in mineral assemblage and some major and trace elements demonstrate that these granites

likely experienced different magma processes (Hu et al., 2011a; Zeng et al., 2011, 2015; Hou et al., 2012; Dai et al., 2020a). Based on geochemical features, the Eocene granites in the Yardoi area can be broadly divided into two major types: high-Mg# granites (HMGs) and low-Mg# granites (LMGs). The HMGs are mainly composed of two-mica granites including several relatively large intrusions such as Yardoi, Dala, Quedang, and a series of sills or dikes, such as Liemai (Figure 2; Zeng et al., 2011, 2015; Hou et al., 2012; Dai et al., 2020a). Thus, these granites show overwhelming superiority in volume. The HMGs are characterized by relatively high contents of TFeO, MgO, Mg#, TiO<sub>2</sub>, P<sub>2</sub>O<sub>5</sub>, LREE, Y, Th, Sr, incompatible elements (Cr and Ni) and Eu/Eu\*, and low contents of SiO<sub>2</sub> and Rb/Sr and Rb/Ba ratios (Figures 6, 9, 11, 12). Typically, the HMGs have high Sr/Y and (La/Yb)<sub>N</sub> values showing adakitic characteristics (Figures 6C, D). Besides, these granites show higher degree of REE differentiation, but less remarkable negative Eu anomalies (Figure 6A). The LMGs consist mainly of minor sub-volcanic leucogranite in Longzi County and leucogranite sills or dikes in Yardoi dome (Hu et al., 2011a; Zeng et al., 2015). These granites are poor in dark minerals and have low Sr/Y and (La/Yb)<sub>N</sub> ratios precluding their adakitic signatures (Figures 6C, D; Hu et al., 2011a; Zeng et al., 2015). In contrast, in spite of less degree of REE differentiation, the LMGs show remarkable negative Eu anomalies (Figure 6A).

The linear correlations between HMGs and LMGs on the Harker diagrams (Figure 12) are indicative of their evolutionary relationship. Especially, more notable negative Eu and Sr anomalies (Figures 6A, B, 12I) of the LMGs demonstrate that the LMGs represent granitic magmas that were evolved from the HMGs by crystal fractionation of plagioclase (Zeng et al., 2015). However, perceptible geochemical discontinuities in the whole-rock geochemistry can be identified between these two granite types (Figure 12), which differs from the continuum in chemical compositions that is commonly assumed to be resulted from a continuous separation of crystals and derivative melts (e.g., Bonnefoi et al., 1995). In addition, generation of high evolved melts through segregation of crystals from a high-silica magma isn't easy due to relatively high viscosity of the silica-rich magma and low-density contrast between the crystals and the liquid. Thus, a simple continuous fractional crystallization process is probably inefficient to interpret the compositional gaps between these two types of granite (Liu et al., 2019).

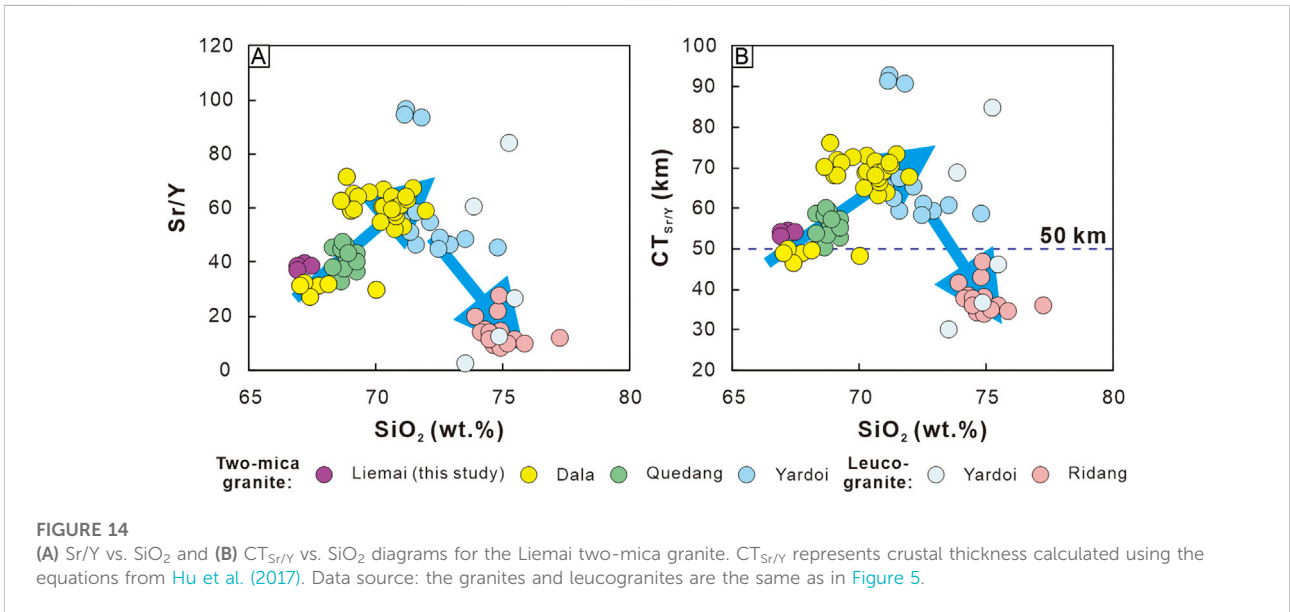
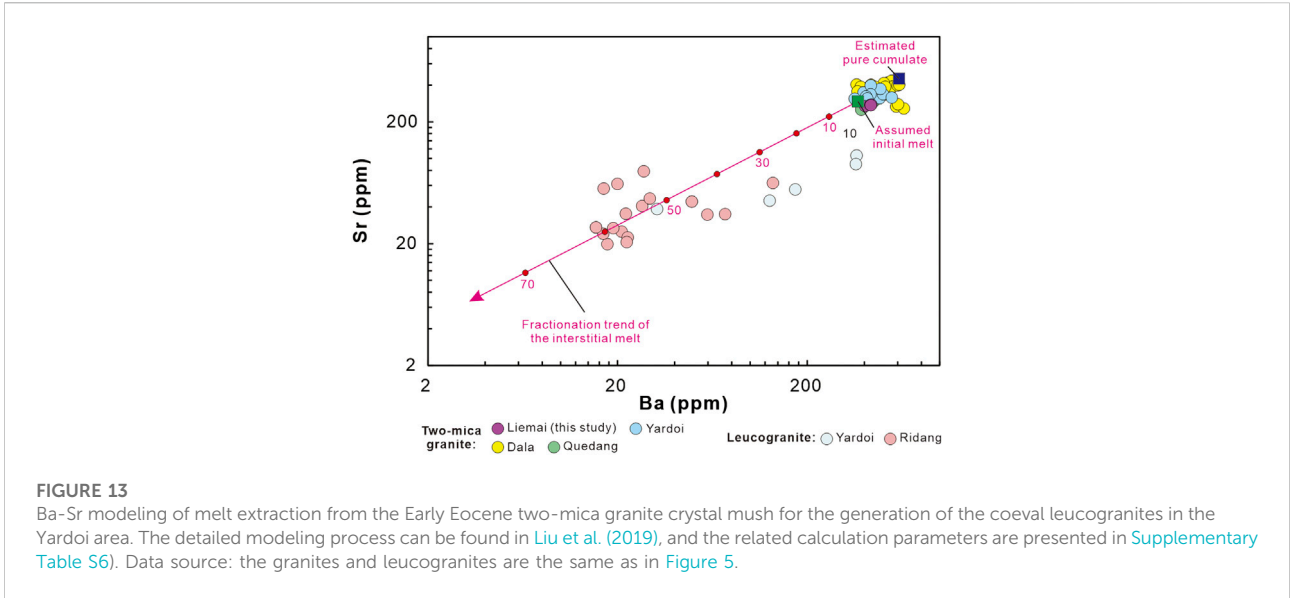
Alternatively, fractional crystallization of a crystal mush (Michael, 1984; Lee and Morton, 2015) has been proposed to interpret the genetic relationships between the less evolved granites and the adjacent highly evolved derivative granites in the Tibet-Himalaya orogen (Liu et al., 2019; Wang et al., 2021). In this model, intensive crystal fractionation is unnecessary. Instead, separation of residual liquid from the crystal mush is enough to generate highly evolved melts (Michael, 1984; Lee and Morton, 2015). Obviously, separation of liquid is much more viable than that of mineral crystals from a crystal mush. Especially, the high



volatile (i.e., H<sub>2</sub>O, F and B) contents can lowered magma solidus and decreased the melt viscosity (Baker and Vaillancourt, 1995; Scaillet et al., 1996; Sirbescu and Nabelek, 2003), allowing sufficient time and melt activity for the extraction of interstitial liquid. REE tetrad effect-like buckling on the chondrite-normalized REE patterns and deviation of Y/Ho, Nb/Ta and Zr/Hf values from the chondrite values indicate an interaction between the melts and volatile-enriched fluids (Hu et al., 2011a; 2011b). Therefore, the crystal mush model is probably a more suitable candidate for interpreting the relationship between the HMGs and LMGs. The less evolved HMGs can be viewed as the crystal mush (crystal cumulate with

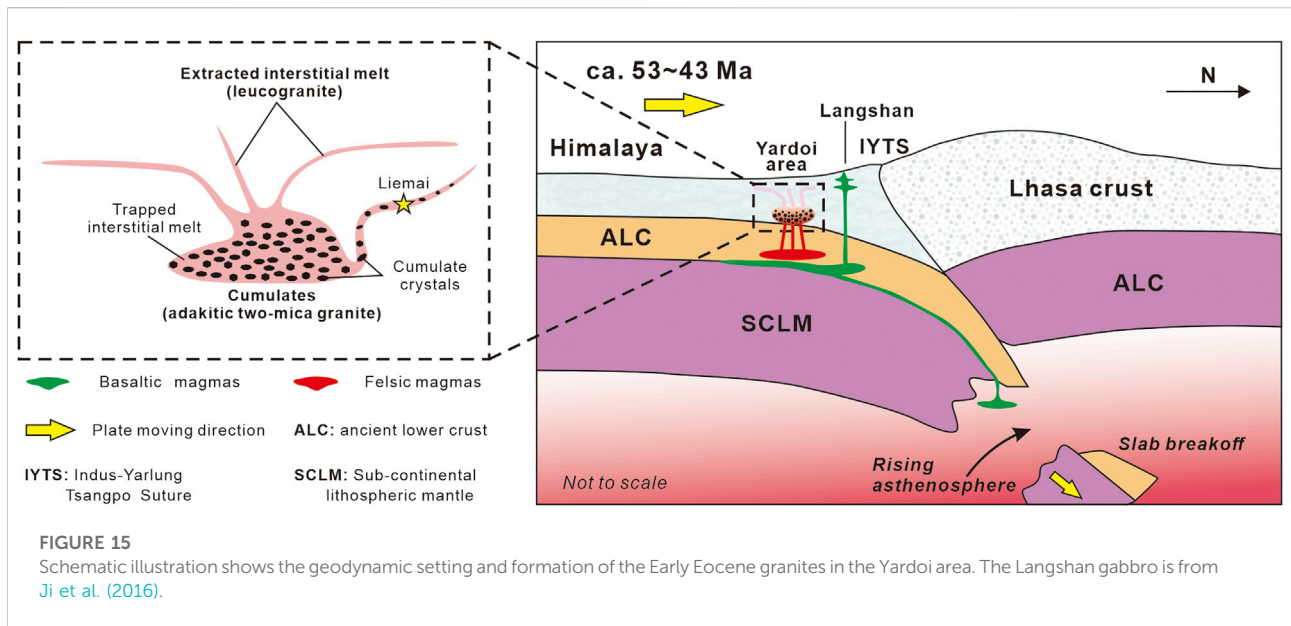
trapped/interstitial melts), whereas the highly evolved LMGs can be regarded as residual liquids extracted from the trapped melts in crystal mush. To assess whether this suggestion is in accordance with the observed geochemical fractionation patterns, we performed trace element modeling on these Eocene granites.

Sr and Ba were selected to verify the fractional crystallization process because their geochemical behaviors are strongly controlled by the main minerals (feldspar and micas) in granites (Liu et al., 2019). The modeling calculations were based on the Rayleigh fractionation equation  $C_L/C_0 = F^{D-1}$ , where  $F_d$  refers to the fraction of the derived liquid,  $D$  refers to the



bulk partition coefficient,  $C_L$  and  $C_0$  refer to the trace element compositions of the fractionated liquid and the initial melt, respectively. The assumed extracted liquid was from the most-evolved LMGs (represented by sample 0473-4 with lowest sum of Ba+Sr from Hu et al., 2011b, Ba = 17.7 ppm, Sr = 19.8 ppm). The average Ba (459.9 ppm) and Sr (362.6 ppm) contents of the HMGs, represent the assumed composition of the residual crystal mush (including data from this study and previously reported data in Zeng et al., 2011, 2015; Hou et al., 2012; Dai et al., 2020a). Partition coefficients for micas were sourced from Icenhower and London (1995) while partition coefficients for

feldspars were sourced from Michael (1984). The detailed calculating process can be found in Liu et al. (2019), and the related calculation parameters are presented in Supplementary Table S6. As illustrated in Figure 13, the theoretical calculations of the evolution of Ba and Sr are broadly in accordance with the actual compositional variations observed in the LMGs. According to the calculation, the most evolved LMGs sample (0473-4) represents the liquid extracted from a crystal mush at crystal fractions of ~60%–63% ( $F_d^{Sr} = 0.37$ ,  $F_d^{Ba} = 0.40$ ; Supplementary Table S6). The other less-evolved LMGs are probably due to involvement of a certain number of cumulate



crystals. In addition, the calculation results show that residual melt trapped in the HMGs crystal mush accounts for ~21%–25% ( $f^{Sr}_{tra} = 0.21$  and  $f^{Ba}_{tra} = 0.25$ ; Supplementary Table S6). Broadly, the results in accordance with previous predictions of a terminal porosity of 20–30 vol% for a residual crystal mush (Lee and Morton, 2015).

Therefore, the modeling calculations based on the Rayleigh fractionation using Sr and Ba indicate that the LMGs were extracted from the HMGs crystal mush at crystal fractions less than or equal to 60%–63%, in which crystal cumulates are plagioclase (41%), K-feldspar (17%), biotite (10%), and muscovite (5%) (Figure 13; Supplementary Table S6). Considering remarkable depletion of LREE and Ti in the LMGs compared to the HMGs, LREE-bearing minerals (e.g., monazite and apatite) and Ti-bearing minerals would have also been cumulative minerals.

### 5.3 Geological implications of the Early Eocene granitoids in eastern Himalaya

A pronounced magmatic flare-up with intensive input of mantle materials along the southern Gangdese at ca. 52–51 Ma (Zhu et al., 2015), together with a sudden drop of the India-Asia convergence rate (Patriat and Achache, 1984; van Hinsbergen et al., 2011), marked the slab breakoff of the subducting Neo-Tethyan oceanic lithosphere. In addition, the crustal thickness beneath the Gangdese reached a thickness >50 km at the beginning of the Eocene (Zhu et al., 2017; Tang et al., 2020). These observations signify that the Neo-Tethys Ocean has been completely closed prior to the Eocene and the Gangdese already had an abnormally thick crust.

Ultra-high pressure metamorphism (~55 Ma) and high amphibolite facies to granulite facies metamorphism (~43–47 Ma) in the Tethyan Himalaya suggest that intensive collision and crustal thickening occurred following closure of the Neo-Tethyan Ocean (Zeng et al., 2011; Gao et al., 2012). This is followed by intensive anatexis of the amphibolitic lower crust to generate Early Eocene adakitic magmas in the Yadoi area (Zeng et al., 2011, 2015; Hou et al., 2012; Dai et al., 2020a). It is worth mentioning that the garnet amphibolites, as the major source rocks for the adakitic rocks, show negligible Eu anomalies and differentiation of REE with low Sr/Y values (< 5) (Figure 6; Hou et al., 2012). In contrast, the garnet amphibolite-derived adakitic rocks are obviously depleted in MREE, HREE and Y, in despite of their comparable LREE and Sr contents and Eu anomalies to the garnet amphibolites (Figure 6). Therefore, MREE-enriched amphibole and HREE-enriched garnet should serve as residual minerals while the plagioclase should serve as melting phase during partial melting to produce melts with remarkable depletion of MREE and HREE and high Sr/Y ratios. Therefore, generation of these Early Eocene adakitic granites in the Yadoi area are indicative of a thickened crust.

In the past, the Sr/Y ratio was used to qualitatively estimate the paleo-crustal thickness. Recently, Chiaradia (2015) found that the Sr/Y ratios of magmatic rocks show positive correlation with crustal thickness in young arcs. Subsequently, Chapman et al. (2015) and Profeta et al. (2015) reconstructed the global and regional correlations between the whole-rock Sr/Y and  $(La/Yb)_N$  ratios of intermediate-felsic arc magmatic rocks and arc crustal thickness, providing quantitative constraints on the paleo-crustal thickness in ancient arcs. More recently, Hu et al. (2017) successfully extended this method to continental collisional zones. The Eocene granites in the Yadoi area were formed

posterior India-Eurasia collision and slab breakoff of the Neo-Tethys oceanic lithosphere thus can be used to estimate the paleo-crustal thickness using the equations from Hu et al. (2017). Interestingly, granite sills (e.g., Liemai two-mica granite) or small intrusions (e.g., Quedang two-mica granite) show relatively lower Sr/Y ratios than big intrusions in Yardoi and Dala (Figure 14A). This is probably because small volume of magmas cooled faster than big ones, thus preserved relatively primitive Sr/Y values. In contrast, magmas with large volume could remain a relative long period at crystal mush state, which could result in elevated Sr/Y ratios due to extraction of low-Sr/Y melts. Therefore, although the extraction of low-Sr/Y melts (LMGs) could have increased the Sr/Y ratios of the crystal mush (HMGs) to some degree (Gao et al., 2021), the small intrusions (e.g., Liemai and Queang two-mica granites) with relatively primitive Sr/Y values can be preferably used to estimate the paleo-crustal thickness. This is supported by the close sample plotting sites of these granites to that of the assumed initial melt in the Sr vs. Ba diagram (Figure 13). The calculated  $CT_{Sr/Y}$  values (crustal thickness based on whole-rock Sr/Y ratios) are broadly range from 50 to 90 km (Figure 14B) using the equation from Hu et al. (2017). Thus, the crustal thickness beneath the Himalaya was inferred to ~50 km during the Early Eocene.

Therefore, both sides of the IYTS experienced notable crustal thickening and gained an abnormally thick crust (~50 km) in the Early Eocene due to the India-Asia collision. Importantly, ascent of hot asthenospheric materials through slab windows caused by slab breakoff of the Neo-Tethys oceanic lithosphere triggered generation of mafic magmas (Ji et al., 2016). Mafic magmas that underplated to the crust-mantle boundary caused partial melting of the thickened lower crust to form adakitic rocks while those intruded in the middle-upper crust formed mafic rocks (Figure 15).

## 6 Conclusion

The following conclusions can be drawn from this study.

- (1) The Liemai two-mica granite was emplaced at ca. 43 Ma similar to adjacent Yardoi, Dala, Quedang two-mica granites, and sub-volcanic leucogranite in Longzi County and leucogranite sills or dikes in Yardoi dome.
- (2) The Liemai two-mica granite, similar to other coeval two-mica granites in the Yardoi area, shows adakitic features and was derived from partial melting of thickened lower crust consisting mainly of garnet amphibolite with minor metapelites.
- (3) The high- and low-Mg# granites in the Yardoi area should be cogenetic. The highly evolved low-Mg granites were extracted from the high-Mg# granitic crystal mush at crystal fractions less than or equal to 52%–53%, in which crystal cumulates are plagioclase, K-feldspar, biotite, muscovite, LREE-bearing minerals (e.g., monazite and apatite) and Ti-bearing minerals.
- (4) Underplating of basaltic magmas triggered by slab breakoff of the Neo-Tethyan oceanic lithosphere was the most possible mechanism supplying heat to induce partial melting of the thickened (~50 km) amphibolitic lower crust in Himalaya orogen to generate granites with adakitic signatures.

## Data availability statement

The original contributions presented in the study are included in the article/Supplementary Material, further inquiries can be directed to the corresponding authors.

## Author contributions

ZD and HC contributed to field investigation, experiments, and writing the manuscript. ZY, GL and YX contributed specifically to funding acquisition and supervision. LD and KG contributed to field investigation.

## Funding

This study was financially supported by the National Natural Science Foundation of China (grant/award numbers: 92155305, 42103066 and 91955208).

## Conflict of interest

The authors declare that the research was conducted in the absence of any commercial or financial relationships that could be construed as a potential conflict of interest.

## Publisher's note

All claims expressed in this article are solely those of the authors and do not necessarily represent those of their affiliated organizations, or those of the publisher, the editors and the reviewers. Any product that may be evaluated in this article, or claim that may be made by its manufacturer, is not guaranteed or endorsed by the publisher.

## Supplementary material

The Supplementary Material for this article can be found online at: <https://www.frontiersin.org/articles/10.3389/feart.2022.1104197/full#supplementary-material>

## References

- Aikman, A. B., Harrison, T. M., and Hermann, J. (2012). The origin of eo- and neo-himalayan granitoids, eastern Tibet. *J. Asian Earth Sci.* 58 (30), 143–157. doi:10.1016/j.jseas.2012.05.018
- Aikman, A. B., Harrison, T. M., and Lin, D. (2008). Evidence for early (>44 Ma) Himalayan crustal thickening, tethyan Himalaya, southeastern Tibet. *Earth Planet. Sci. Lett.* 274 (1–2), 14–23. doi:10.1016/j.epsl.2008.06.038
- Baker, D. R., and Vaillancourt, J. (1995). The low viscosities of F+ H<sub>2</sub>O-bearing granitic melts and implications for melt extraction and transport. *Earth Planet. Sci. Lett.* 132 (1–4), 199–211. doi:10.1016/0012-821x(95)00054-g
- Batchelor, R. A., and Bowden, P. (1985). Petrogenetic interpretation of granitoid rock series using multicationic parameters. *Chem. Geol.* 48 (1–4), 43–55. doi:10.1016/0009-2541(85)90034-8
- Blichert-Toft, J., Chauvel, C., and Albarède, F. (1997). Separation of Hf and Lu for high-precision isotope analysis of rock samples by magnetic sector-multiple collector ICP-MS. *Contributions Mineralogy Petrology* 127 (3), 248–260. doi:10.1007/s004100050278
- Bonnefoi, C., and Provost, A. (1995). The 'Daly gap' as a magmatic catastrophe. *Nature* 378, 270–272. doi:10.1038/378270a0
- Cao, H. W., Huang, Y., Li, G. M., Zhang, L. K., Wu, J. Y., Dong, L., et al. (2018). Late triassic sedimentary records in the northern tethyan Himalaya: Tectonic link with greater India. *Geosci. Front.* 9 (1), 273–291. doi:10.1016/j.gsf.2017.04.001
- Cao, H. W., Li, G. M., Zhang, L. K., Dong, L., Gao, K., and Dai, Z. W. (2020). Monazite U-Th-Pb age of Liemai Eocene granites in the southern Tibet and its geological implications. *Sediment. Geol. Tethyan Geol.* 40 (2), 31–42. (in Chinese with English abstract). doi:10.19826/j.cnki.1009-3850.(2020)02-0031-12
- Cao, K., Yang, Z. M., White, N. C., and Hou, Z. Q. (2022a). Generation of the giant porphyry Cu-Au deposit by repeated recharge of mafic magmas at pulung in eastern Tibet. *Econ. Geol.* 117 (1), 57–90. doi:10.5382/econgeo.4860
- Cao, H. W., Pei, Q. M., Santosh, M., Li, G. M., Zhang, L. K., Zhang, X. F., et al. (2022b). Himalayan leucogranites: A review of geochemical and isotopic characteristics, timing of formation, Genesis, and rare metal mineralization. *Earth-Science Rev.* 234, 104229. doi:10.1016/j.earscirev.2022.104229
- Castillo, P. R., Janney, P. E., and Solidum, R. U. (1999). Petrology and geochemistry of camiguin island, southern Philippines: Insights to the source of adakites and other lavas in a complex arc setting. *Contributions mineralogy petrology* 134, 33–51. doi:10.1007/s004100050467
- Chapman, J. B., Ducea, M. N., DeCelles, P. G., and Profeta, L. (2015). Tracking changes in crustal thickness during orogenic evolution with Sr/Y: An example from the North American Cordillera. *Geology* 43 (10), 919–922. doi:10.1130/g36996.1
- Chappell, B. W., and White, A. J. R. (1992). I- and S-type granites in the lachlan fold belt. *Earth Environ. Sci. Trans. R. Soc. Edinb.* 83 (1–2), 1–26. doi:10.1017/S0263593300007720
- Chen, J. L., Wu, J. B., Xu, J. F., Dong, Y. H., Wang, B. D., and Kang, Z. Q. (2013). Geochemistry of Eocene high-Mg# adakitic rocks in the northern Qiangtang terrane, central Tibet: Implications for early uplift of the plateau. *Geol. Soc. Am. Bull.* 125 (11–12), 1800–1819. doi:10.1130/b30755.1
- Chiaradia, M. (2015). Crustal thickness control on Sr/Y signatures of recent arc magmas: An earth scale perspective. *Sci. Rep.* 5, 8115. doi:10.1038/srep08115
- Chu, G. B., Chen, H. Y., Falloon, T. J., Han, J. S., Zhang, S. T., Cheng, J. M., et al. (2020). Early cretaceous mantle upwelling and melting of juvenile lower crust in the middle-lower yangtze river metallogenic belt: Example from tongshankou Cu-(Mo W) ore deposit. *Gondwana Res.* 83, 183–200. doi:10.1016/j.gr.2020.02.004
- Chung, S. L., Liu, D. Y., Ji, J. Q., Chu, M. F., Lee, H. Y., Wen, D. J., et al. (2003). Adakites from continental collision zones: Melting of thickened lower crust beneath southern Tibet. *Geology* 31 (11), 1021–1024. doi:10.1130/g19796.1
- Cottle, J. M., Searle, M. P., Jessup, M. J., Crowley, J. L., and Law, R. D. (2015). Rongbuk re-visited: Geochronology of leucogranites in the footwall of the south Tibetan detachment system, everest region, southern Tibet. *Lithos* 227, 94–106. doi:10.1016/j.lithos.2015.03.019
- Dai, Z. W., Dong, L., Li, G. M., Huizenga, J. M., Ding, J., Zhang, L. K., et al. (2020a). Crustal thickening prior to 43 Ma in the Himalaya: Evidence from lower crust-derived adakitic magmatism in Dala, eastern tethyan Himalaya, Tibet. *Geol. J.* 55 (5), 4021–4046. doi:10.1002/gj.3639
- Dai, Z. W., Huang, H. X., Li, G. M., Huizenga, J. M., Santosh, M., Cao, H. W., et al. (2020b). Formation of Late Cretaceous high-Mg granitoid porphyry in central Lhasa, Tibet: Implications for crustal thickening prior to India-Asia collision. *Geol. J.* 55 (10), 6696–6717. doi:10.1002/gj.3834
- Dai, Z. W., Li, G. M., Ding, J., Huang, Y., and Cao, H. W. (2018). Late cretaceous adakite in Nuri area, Tibet: Products of ridge subduction. *Earth Sci.* 43 (8), 2727–2741. (in Chinese with English abstract). doi:10.3799/dqkx.2018.230
- Davidson, J., Turner, S., Handley, H., Macpherson, C., and Dosseto, A. (2007). Amphibole "sponge" in arc crust? *Geology* 35 (9), 787. doi:10.1130/g23637a.1
- Defant, M. J., and Drummond, M. S. (1990). Derivation of some modern arc magmas by melting of young subducted lithosphere. *Nature* 347 (6294), 662–665. doi:10.1038/347662a0
- Depaolo, D. J. (1988). Age dependence of the composition of continental crust: Evidence from Nd isotopic variations in granitic rocks. *Earth Planet. ence Lett.* 90 (3), 263–271. doi:10.1016/0012-821x(88)90130-6
- Depaolo, D. J., Linn, A. M., and Schubert, G. (1991). The continental crustal age distribution: Methods of determining mantle separation ages from Sm-Nd isotopic data and application to the southwestern United States. *J. Geophys. Res.* 96, 2071. doi:10.1029/90jb02219
- Dolgoplova, A., Seltmann, R., Armstrong, R., Belousova, E., Pankhurst, R. J., and Kavalieris, I. (2013). Sr-Nd-Pb-Hf isotope systematics of the Hugo Dummett Cu-Au porphyry deposit (Oyu Tolgoi, Mongolia). *Lithos* 164–167, 47–64. doi:10.1016/j.lithos.2012.11.017
- Fisher, C. M., Vervoort, J. D., and Hanchar, J. M. (2014). Guidelines for reporting zircon Hf isotopic data by LA-MC-ICPMS and potential pitfalls in the interpretation of these data. *Chem. Geol.* 363, 125–133. doi:10.1016/j.chemgeo.2013.10.019
- Fu, J. G., Li, G. M., Wang, G. H., Zhang, L. K., Liang, W., Zhang, X. Q., et al. (2020). Structural analysis of sheath folds and geochronology in the cuonadong dome, southern Tibet, China: New constraints on the timing of the south Tibetan detachment system and its relationship to North Himalayan gneiss domes. *Terra nova.* 32 (4), 300–323. doi:10.1111/ter.12462
- Gao, J. F., Lu, J. J., Lai, M. Y., Lin, Y. P., and Pu, W. (2003). Analysis of trace elements in rock samples using HR-ICPMS. *J. Nanjing Univ. Nat. Sci.* 39 (6), 844–850. (in Chinese with English abstract).
- Gao, L. E., Zeng, L. S., and Xie, K. J. (2012). Eocene high grade metamorphism and crustal anatexis in the North Himalaya gneiss domes, southern Tibet. *Chin. Sci. Bull.* 57 (6), 639–650. doi:10.1007/s11434-011-4805-4
- Gao, P., Zheng, Y. F., Yakymchuk, C., Zhao, Z. F., and Meng, Z. Y. (2021). The effects of source mixing and fractional crystallization on the composition of Eocene granites in the Himalayan Orogen. *J. Petrology* 62 (7), 1–23. doi:10.1093/petrology/egab037
- Gao, S., Rudnick, R. L., Yuan, H. L., Liu, X. M., Liu, Y. S., Xu, W. L., et al. (2004). Recycling lower continental crust in the North China craton. *Nature* 432, 892–897. doi:10.1038/nature03162
- Grimes, C. B., John, B. E., Kelemen, P. B., Mazdab, F. K., Wooden, J. L., Cheadle, M. J., et al. (2007). Trace element chemistry of zircons from oceanic crust: A method for distinguishing detrital zircon provenance. *Geology* 35 (7), 643–646. doi:10.1130/g23603a.1
- Harris, N. B. W., Pearce, J. A., and Tindle, A. G. (1986). Geochemical characteristics of collision-zone magmatism. *Geol. Soc. Lond. Spec. Publ.* 19, 67–81. doi:10.1144/gsl.sp.1986.019.01.04
- Harrison, T. M., Grove, M., McKeegan, K. D., Coath, C. D., Lovera, O. M., and Fort, P. L. (1999). Origin and episodic emplacement of the manaslu intrusive complex, central Himalaya. *J. Petrology* 40 (1), 3–19. doi:10.1093/ptro/40.1.3
- Hoskin, P. W. O. (2005). Trace-element composition of hydrothermal zircon and the alteration of Hadean zircon from the Jack Hills, Australia. *Geochimica Cosmochimica Acta* 69 (3), 637–648. doi:10.1016/j.gca.2004.07.006
- Hou, Z. Q., Duan, L. F., Lu, Y. J., Zheng, Y. C., Zhu, D. C., Yang, Z. M., et al. (2015). Lithospheric architecture of the Lhasa terrane and its control on ore deposits in the himalayan-Tibetan orogen. *Econ. Geol.* 110 (6), 1541–1575. doi:10.2113/econgeo.110.6.1541
- Hou, Z. Q., Gao, Y. F., Qu, X. M., Rui, Z. Y., and Mo, X. X. (2004). Origin of adakitic intrusives generated during mid-Miocene east-west extension in southern Tibet. *Earth Planet. Sci. Lett.* 220 (1–2), 139–155. doi:10.1016/s0012-821x(04)00007-x
- Hou, Z. Q., Pan, G. T. W., An, J., Mo, X. X., Tian, S. H., Sun, X. M., et al. (2006a). Metallogenesis in Tibetan collisional orogenic belt: II. Mineralization in late-collisional transformation setting. *Mineral. Deposits* 25 (5), 521–543. (in Chinese with English abstract).
- Hou, Z. Q., Yang, Z. S., Xu, W. Y., Mo, X. X., Ding, L., Gao, Y. F., et al. (2006b). Metallogenesis in Tibetan collisional orogenic belt: I. Mineralization in main collisional orogenic setting. *Mineral. Deposits* 25 (4), 337–358. (in Chinese with English abstract).

- Hou, Z. Q., Zheng, Y. C., Zeng, L. S., Gao, L. E., Huang, K. X., Li, W., et al. (2012). Eocene–Oligocene granulites in southern Tibet: Constraints on crustal anatexis and tectonic evolution of the Himalayan orogen. *Earth Planet. Sci. Lett.* 349 (350), 38–52. doi:10.1016/j.epsl.2012.06.030
- Hu, F. Y., Ducea, M. N., Liu, S. W., and Chapman, J. B. (2017). Quantifying crustal thickness in continental collisional belts: Global perspective and a geologic application. *Sci. Rep.* 7, 7058. doi:10.1038/s41598-017-07849-7
- Hu, G. Y., Zeng, L. S., and Qi, X. X. (2011a). The mid-eocene subvolcanic field in the lhunze-qiaga area, tethyan Himalaya, southern Tibet: A high-level magmatic suite related to the yardio two-mica granite. *Acta Petrol. Sin.* 27 (11), 3308–3318. (in Chinese with English abstract).
- Hu, G. Y., Zeng, L. S., Gao, L. E., and Xie, K. J. (2011b). Lanthanide kinked shape, similar to Tetrad effect, observed in sub-volcanic rocks from Qiaga, southern Tibet, China. *Geol. Bull. China* 30 (1), 82–94. (in Chinese with English abstract).
- Hu, Z. C., Liu, Y. S., Gao, S., Liu, W. G., Zhang, W., Tong, X. R., et al. (2012). Improved *in situ* Hf isotope ratio analysis of zircon using newly designed X skimmer cone and jet sample cone in combination with the addition of nitrogen by laser ablation multiple collector ICP-MS. *J. Anal. Atomic Spectrom.* 27, 1391–1399. doi:10.1039/c2ja30078h
- Hu, Z. C., Zhang, W., Liu, Y. S., Gao, S., Li, M., Zong, K. Q., et al. (2015). “Wave” signal-smoothing and mercury-removing device for laser ablation quadrupole and multiple collector ICPMS analysis: Application to lead isotope analysis. *Anal. Chem.* 87 (2), 1152–1157. doi:10.1021/ac503749k
- Icenhower, J., and London, D. (1995). An experimental study of element partitioning among biotite, muscovite, and coexisting peraluminous silicic melt at 200 MPa (H<sub>2</sub>O). *Am. Mineralogist* 80 (11–12), 1229–1251. doi:10.2138/am-1995-11-1213
- Inger, S., and Harris, N. (1993). Geochemical constraints on leucogranite magmatism in the langtang valley, Nepal Himalaya. *J. Petrology* 34 (2), 345–368. doi:10.1093/petrology/34.2.345
- Ji, W. Q., Wu, F. Y., Chung, S. L., Wang, X. C., Liu, C. Z., Li, Q. L., et al. (2016). Eocene Neo-Tethyan slab breakoff constrained by 45 Ma oceanic island basalt-type magmatism in southern Tibet. *Geology* 44 (4), 283–286. doi:10.1130/g37612.1
- Jiang, Z. Q., Wang, Q., Li, Z. X., Wyman, D. A., Tang, G. J., Jia, X. H., et al. (2012). Late Cretaceous (ca. 90 Ma) adakitic intrusive rocks in the Kelu area, Gangdese Belt (southern Tibet): Slab melting and implications for Cu–Au mineralization. *J. Asian Earth Sci.* 53, 67–81. doi:10.1016/j.jseas.2012.02.010
- Jiang, Z. Q., Wang, Q., Wyman, D. A., Tang, G. J., Jia, X. H., Yang, Y. H., et al. (2011). Origin of ~30Ma chongmuda adakitic intrusive rocks in the southern gangdese region, southern Tibet: Partial melting of the northward subducted Indian continent crust? *Geochimica* 40 (2), 126–146. (in Chinese with English abstract). doi:10.19700/j.0379-1726.2011.02.002
- Karsli, O., Dokuz, A., Uysal, I., Aydin, F., Kandemir, R., and Wijbrans, J. (2010). Generation of the early Cenozoic adakitic volcanism by partial melting of mafic lower crust, eastern Turkey; implications for crustal thickening to delamination. *Lithos* 114 (1–2), 109–120. doi:10.1016/j.lithos.2009.08.003
- Klein, E. M. (2004). “Geochemistry of the igneous oceanic crust,” in *Treatise on geochemistry*. Editor H. D. Holland and K. K. Turekian. Amsterdam: Elsevier 3, 433–463.
- Kohn, M. J. (2014). Himalayan metamorphism and its tectonic implications. *Annu. Rev. Earth Planet. Sci.* 42, 381–419. doi:10.1146/annurev-earth-060313-055005
- Lai, S. C., and Qin, J. F. (2013). Adakitic rocks derived from the partial melting of subducted continental crust: Evidence from the Eocene volcanic rocks in the northern Qiangtang block. *Gondwana Res.* 23 (2), 812–824. doi:10.1016/j.gr.2012.06.003
- Lee, C.-T. A., and Morton, D. M. (2015). High silica granites: Terminal porosity and crystal settling in shallow magma chambers. *Earth Planet. Sci. Lett.* 409, 23–31. doi:10.1016/j.epsl.2014.10.040
- Leloup, P. H., Mahéo, G., Arnaud, N., Kali, E., Boutonnet, E., Liu, D., et al. (2010). The South Tibet detachment shear zone in the Dinggye area: Time constraints on extrusion models of the Himalayas. *Earth Planet. Sci. Lett.* 292 (1–2), 1–16. doi:10.1016/j.epsl.2009.12.035
- Li, W. K., Yang, Z. M., Chiaradia, M., Lai, Y., and Zhang, J. Y. (2020). Redox state of southern Tibetan upper mantle and ultrapotassic magmas. *Geology* 48 (7), 733–736. doi:10.1130/g47411.1
- Liu, Y. S., Gao, S., Hu, Z. C., Gao, C. G., Zong, K. Q., and Wang, D. B. (2010). Continental and oceanic crust recycling-induced melt–peridotite interactions in the trans-north China orogen: U–Pb dating, Hf isotopes and trace elements in zircons from mantle xenoliths. *J. Petrology* 51 (1–2), 537–571. doi:10.1093/petrology/egp082
- Liu, Y. S., Hu, Z. C., Gao, S., Günther, D., Xu, J., Gao, C. G., et al. (2008). *In situ* analysis of major and trace elements of anhydrous minerals by LA-ICP-MS without applying an internal standard. *Chem. Geol.* 257 (1–2), 34–43. doi:10.1016/j.chemgeo.2008.08.004
- Liu, Z. C., Wu, F. Y., Liu, X. C., Wang, J. G., Yin, R., Qiu, Z. L., et al. (2019). Mineralogical evidence for fractionation processes in the Himalayan leucogranites of the Ramba Dome, southern Tibet. *Lithos* 340–341, 71–86. doi:10.1016/j.lithos.2019.05.004
- Liu, Z. C., Wu, F. Y., Qiu, Z. L., Wang, J. G., Liu, X. C., Ji, W. Q., et al. (2017). Leucogranite geochronological constraints on the termination of the South Tibetan Detachment in eastern Himalaya. *Tectonophysics* 721, 106–122. doi:10.1016/j.tecto.2017.08.019
- Long, X. P., Wilde, S. A., Wang, Q., Yuan, C., Wang, X. C., Li, J., et al. (2015). Partial melting of thickened continental crust in central Tibet: Evidence from geochemistry and geochronology of Eocene adakitic rhyolites in the northern Qiangtang Terrane. *Earth Planet. Sci. Lett.* 414, 30–44. doi:10.1016/j.epsl.2015.01.007
- Ludwig, K. R. (2003). User’s manual for a geochronological toolkit for Microsoft Excel (Isoplot/Ex version 3.0). *Spec. Publ.* 4, 1–71.
- Luffi, P., and Ducea, M. N. (2022). Chemical mohometry: Assessing crustal thickness of ancient orogens using geochemical and isotopic data. *Rev. Geophys.* 60 (2), 1–42. doi:10.1029/2021rg000753
- Ma, L., Wang, B. D., Jiang, Z. Q., Wang, Q., Li, Z. X., Wyman, D. A., et al. (2014). Petrogenesis of the early eocene adakitic rocks in the napuri area, southern Lhasa: Partial melting of thickened lower crust during slab break-off and implications for crustal thickening in southern Tibet. *Lithos* 196–197, 321–338. doi:10.1016/j.lithos.2014.02.011
- Ma, L., Wang, Q., Wyman, D. A., Li, Z. X., Jiang, Z. Q., Yang, J. H., et al. (2013). Late Cretaceous (100–89 Ma) magnesian charnockites with adakitic affinities in the Milin area, eastern Gangdese: Partial melting of subducted oceanic crust and implications for crustal growth in southern Tibet. *Lithos* 175–176, 315–332. doi:10.1016/j.lithos.2013.04.006
- Macpherson, C. G., Dreher, S. T., and Thirlwall, M. F. (2006). Adakites without slab melting: High pressure differentiation of island arc magma, Mindanao, the Philippines. *Earth Planet. Sci. Lett.* 243, 581–593. doi:10.1016/j.epsl.2005.12.034
- Maniar, P. D., and Piccoli, P. M. (1989). Tectonic discrimination of granulites. *Geol. Soc. Am. Bull.* 101 (5), 635–643. doi:10.1130/0016-7606(1989)101<0635:tdog>2.3.co;2
- Martin, H. (1986). Effect of steeper Archean geothermal gradient on geochemistry of subduction-zone magmas. *Geology* 14 (9), 753–756. doi:10.1130/0091-7613(1986)14<753:eosagg>2.0.co;2
- Michael, P. J. (1984). Chemical differentiation of the Cordillera Paine granite (southern Chile) by *in situ* fractional crystallization. *Contributions Mineralogy Petrology* 87 (2), 179–195. doi:10.1007/bf00376223
- Middlemost, E. A. K. (1994). Naming materials in the magma/igneous rock system. *Earth-Science Rev.* 37 (3), 215–224. doi:10.1016/0012-8252(94)90029-9
- Mo, X. X., Hou, Z. Q., Niu, Y. L., Dong, G. C., Qu, X. M., Zhao, Z. D., et al. (2007). Mantle contributions to crustal thickening during continental collision: Evidence from Cenozoic igneous rocks in southern Tibet. *Lithos* 96 (1–2), 225–242. doi:10.1016/j.lithos.2006.10.005
- Mo, X. X. (2011). Magmatism and evolution of the Tibetan plateau. *Geol. J. China Univ.* 17 (3), 351–367. (in Chinese with English abstract). doi:10.16108/j.issn1006-7493.2011.03.004
- Moyen, J.-F. (2009). High Sr/Y and La/Yb ratios: The meaning of the “adakitic signature”. *Lithos* 112 (3), 556–574. doi:10.1016/j.lithos.2009.04.001
- Myrow, P. M., Fike, D. A., Malmkog, E., Leslie, S. A., Zhang, T., Singh, B. P., et al. (2019). Ordovician–Silurian boundary strata of the Indian Himalaya: Record of the latest ordoevian boda event. *Geol. Soc. Am. Bull.* 131 (5–6), 881–898. doi:10.1130/b31860.1
- Niu, X. L., Zhao, Z. D., Mo, X. X., DePaolo, D., Dong, G. C., Zhang, S. Q., et al. (2006). Elemental and Sr–Nd–Pb isotopic geochemistry for basic rocks from decunangren ophiolites in xigaze area, Tibet: Implications for the characteristics of the tethyan upper mantle domain. *Acta Petrol. Sin.* 22 (12), 2875–2888. (in Chinese with English abstract).
- Pan, G. T., Wang, L. Q., Li, R. S., Yuan, S. H., Ji, W. H., Yin, F. G., et al. (2012). Tectonic evolution of the Qinghai–Tibet Plateau. *J. Asian Earth Sci.* 53, 3–14. doi:10.1016/j.jseas.2011.12.018
- Parrish, R. R. (1990). U–Pb dating of monazite and its application to geological problems. *Can. J. Earth Sci.* 27 (11), 1431–1450. doi:10.1139/e90-152
- Patriat, P., and Achahe, J. (1984). India-Eurasia collision chronology has implications for crustal shortening and driving mechanism of plates. *Nature* 311 (5987), 615–621. doi:10.1038/311615a0
- Pearce, J. A., Harris, N. B., and Tindle, A. G. (1984). Trace element discrimination diagrams for the tectonic interpretation of granitic rocks. *J. petrology* 25 (4), 956–983. doi:10.1093/petrology/25.4.956

- Peccerillo, A., and Taylor, S. R. (1976). Geochemistry of eocene calc-alkaline volcanic rocks from the Kastamonu area, Northern Turkey. *Contributions Mineralogy Petrology* 58, 63–81. doi:10.1007/bf00384745
- Profeta, L., Ducea, M. N., Chapman, J. B., Paterson, S. R., Gonzales, S. M., Kirsch, M., et al. (2015). Quantifying crustal thickness over time in magmatic arcs. *Sci. Rep.* 5, 17786. doi:10.1038/srep17786
- Qi, X. X., Zeng, L. S., Meng, X. J., Xu, Z. Q., and Li, T. F. (2008). Zircon SHRIMP U-Pb dating for Dala granite in the Tethyan Himalaya and its geological implication. *Acta Petrol. Sin.* 24 (7), 1501–1508. (in Chinese with English abstract).
- Rapp, R. P., Shimizu, N., Norman, M. D., and Applegate, G. S. (1999). Reaction between slab-derived melts and peridotite in the mantle wedge: Experimental constraints at 3.8 GPa. *Chem. Geol.* 160, 335–356. doi:10.1016/s0009-2541(99)00106-0
- Rapp, R. P., Xiao, L., and Shimizu, N. (2002). Experimental constraints on the origin of potassium-rich adakites in eastern China. *Acta Petrol. Sin.* 18 (3), 293–302.
- Richards, A., Argles, T., Harris, N., Parrish, R., Ahmad, T., Darbyshire, F., et al. (2005). Himalayan architecture constrained by isotopic tracers from clastic sediments. *Earth Planet. Sci. Lett.* 236 (3–4), 773–796. doi:10.1016/j.epsl.2005.05.034
- Rickwood, P. C. (1989). Boundary lines within petrologic diagrams which use oxides of major and minor elements. *Lithos* 22 (4), 247–263. doi:10.1016/0024-4937(89)90028-5
- Rudnick, R. L., and Gao, S. (2003). “Composition of the continental crust,” in *Treatise on geochemistry*. Editor K. K. Turekian (Oxford: Pergamon), 1–64.
- Scaillet, B., Holtz, F., Pichavant, M., and Schmidt, M. (1996). Viscosity of Himalayan leucogranites: Implications for mechanisms of granitic magma ascent. *J. Geophys. Res. Solid Earth* 101 (B12), 27691–27699. doi:10.1029/96jb01631
- Sirbescu, M.-L. C., and Nabelek, P. I. (2003). Crustal melts below 400 C. *Geology* 31 (8), 685–688. doi:10.1130/g19497.1
- Streck, M. J., Leeman, W. P., and Chesley, J. (2007). High-magnesian andesite from Mount Shasta: A product of magma mixing and contamination, not a primitive mantle melt. *Geology* 35 (4), 351–354. doi:10.1130/g23286a.1
- Sun, S. S., and McDonough, W. F. (1989). Chemical and isotopic systematics of oceanic basalts: Implications for mantle composition and processes. *Geol. Soc. Lond. Spec. Publ.* 42, 313–345. doi:10.1144/gsl.sp.1989.042.01.19
- Sylvester, P. J. (1998). Post-collisional strongly peraluminous granites. *Lithos* 45 (1–4), 29–44. doi:10.1016/s0024-4937(98)00024-3
- Tang, M., Ji, W. Q., Chu, X., Wu, A. B., and Chen, C. (2020). Reconstructing crustal thickness evolution from europium anomalies in detrital zircons. *Geology* 49 (1), 76–80. doi:10.1130/g47745.1
- Tian, L. M., Wang, L. Y., Zheng, H. T., and Yang, B. (2018). Eocene magmatism from the Liemai intrusion in the eastern tethyan himalayan belt and tectonic implications. *Geol. Mag.* 156, 510–524. doi:10.1017/s0016756817000966
- van Hinsbergen, D. J. J., Steinberger, B., Doubrovine, P. V., and Gassmöller, R. (2011). Acceleration and deceleration of India-Asia convergence since the Cretaceous: Roles of mantle plumes and continental collision. *J. Geophys. Res.* 116 (B6), B06101. doi:10.1029/2010jb008051
- Vidal, P., Cocherie, A., and Le Fort, P. (1982). Geochemical investigations of the origin of the Manaslu leucogranite (Himalaya, Nepal). *Geochimica Cosmochimica Acta* 46 (11), 2279–2292. doi:10.1016/0016-7037(82)90201-0
- Wang, L. Q., Cheng, W. B., Gao, T., and Wang, Y. (2021). A model involving amphibolite lower crust melting and subsequent melt extraction for leucogranite generation. *GSA Bull.* 134, 1160–1179. doi:10.1130/b36055.1
- Wang, Q., Xu, J. F., Jian, P., Bao, Z. W., Zhao, Z. H., Li, C. F., et al. (2006). Petrogenesis of adakitic porphyries in an extensional tectonic setting, dexing, south China: Implications for the genesis of porphyry copper mineralization. *J. Petrology* 47 (1), 119–144. doi:10.1093/petrology/egi070
- Wang, Q., Zhu, D. C., Zhao, Z. D., Liu, S. A., Chung, S. L., Li, S. M., et al. (2014). Origin of the ca. 90Ma magnesia-rich volcanic rocks in SE Nyima, central Tibet: Products of lithospheric delamination beneath the Lhasa-Qiangtang collision zone. *Lithos* 198–199, 24–37. doi:10.1016/j.lithos.2014.03.019
- Wang, Y. J., Wang, X. S., Bi, X. W., Tao, Y., and Lan, T. G. (2020). Intraplate adakite-like rocks formed by differentiation of mantle-derived mafic magmas: A case study of eocene intermediate-felsic porphyries in the machangqing porphyry Cu-Au mining district, se Tibetan plateau. *J. Asian Earth Sci.* 196, 104364. doi:10.1016/j.jseas.2020.104364
- Woodhead, J., Hergt, J., Shelley, M., Eggins, S., and Kemp, R. (2004). Zircon Hf-isotope analysis with an excimer laser, depth profiling, ablation of complex geometries, and concomitant age estimation. *Chem. Geol.* 209 (1–2), 121–135. doi:10.1016/j.chemgeo.2004.04.026
- Wu, F. Y., Li, X. H., Zheng, Y. F., and Gao, S. (2007). Lu-Hf isotopic systematics and their applications in petrology. *Acta Petrol. Sin.* 23 (2), 185–220. (in Chinese with English abstract).
- Wu, F. Y., Liu, X. C., Liu, Z. C., Wang, R. C., Xie, L., Wang, J. M., et al. (2020). Highly fractionated Himalayan leucogranites and associated rare-metal mineralization. *Lithos* 352–353, 105319. doi:10.1016/j.lithos.2019.105319
- Wu, F. Y., Liu, Z. C., Liu, X. C., and Ji, W. Q. (2015). Himalayan leucogranite: Petrogenesis and implications to orogenesis and plateau uplift. *Acta Petrol. Sin.* 31 (1), 1–36. (in Chinese with English abstract).
- Wu, Y. B., and Zheng, Y. F. (2004). Genesis of zircon and its constraints on interpretation of U-Pb age. *Chin. Sci. Bull.* 49 (15), 1554–1569. doi:10.1360/04wd0130
- Wu, Z. H., Ye, P. S., Wu, Z. H., and Zhao, Z. (2014). LA-ICP-MS zircon U-Pb ages of tectonic-thermal events in the Yalaxiangbo dome of Tethys Himalayan belt. *Geol. Bull. China* 33 (5), 595–605. (in Chinese with English abstract).
- Xu, J. F., and Castillo, P. R. (2004). Geochemical and Nd-Pb isotopic characteristics of the tethyan asthenosphere: Implications for the origin of the Indian ocean mantle domain. *Tectonophysics* 393 (1–4), 9–27. doi:10.1016/j.tecto.2004.07.028
- Xu, J. F., Shinjo, R., Defant, M. J., Wang, Q., and Rapp, R. P. (2002). Origin of Mesozoic adakitic intrusive rocks in the Ningzhen area of east China: Partial melting of delaminated lower continental crust? *Geology* 30 (12), 1111–1114. doi:10.1130/0091-7613(2002)030<1111:oomair>2.0.co;2
- Xu, W. L., Wang, Q. H., Wang, D. Y., Guo, J. H., and Pei, F. P. (2006). Mesozoic adakitic rocks from the Xuzhou–Suzhou area, eastern China: Evidence for partial melting of delaminated lower continental crust. *J. Asian Earth Sci.* 27, 230–240. doi:10.1016/j.jseas.2005.03.005
- Yang, D. B., Xu, W. L., Zhao, G. C., Huo, T. F., Shi, J. P., and Yang, H. T. (2016b). Tectonic implications of Early Cretaceous low-Mg adakitic rocks generated by partial melting of thickened lower continental crust at the southern margin of the central North China Craton. *Gondwana Res.* 38, 220–237. doi:10.1016/j.gr.2015.11.013
- Yang, X. S., and Jin, Z. M. (2001). Studies on Rb-Sr and Sm-Nd isotope of yadong leucogranite in Tibet: Constraint on its age and source material. *Geol. Rev.* 47 (3), 294–300. (in Chinese with English abstract). doi:10.16509/j.georeview.2001.03.013
- Yang, Z. M., Chang, Z. S., Paquette, J., White, N. C., Hou, Z. Q., and Ge, L. S. (2015a). Magmatic Au mineralization at the Bilie Au deposit, China. *Econ. Geol.* 110 (7), 1661–1668. doi:10.2113/econgeo.110.7.1661
- Yang, Z. M., Lu, Y. J., Hou, Z. Q., and Chang, Z. S. (2015b). High-Mg diorite from Qulong in southern Tibet: Implications for the Genesis of adakite-like intrusions and associated porphyry Cu deposits in collisional orogens. *J. Petrology* 56, 227–254. doi:10.1093/petrology/egu076
- Yang, Z. M., Goldfarb, R. J., and Chang, Z. S. (2016a). Generation of postcollisional porphyry copper deposits in southern Tibet triggered by subduction of the Indian continental plate. *Soc. Econ. Geol. Spec. Pub.* 19, 279–300. doi:10.5382/SP.19.11
- Yin, A. (2006). Cenozoic tectonic evolution of the Himalayan orogen as constrained by along-strike variation of structural geometry, exhumation history, and foreland sedimentation. *Earth-Science Rev.* 76 (1–2), 1–131. doi:10.1016/j.earscirev.2005.05.004
- Yin, A., and Harrison, T. M. (2000). Geologic evolution of the Himalayan-Tibetan orogen. *Annu. Rev. Earth Planet. Sci.* 28, 211–280. doi:10.1146/annurev.earth.28.1.211
- Zeng, L. S., Gao, L. E., Dong, C. Y., and Tang, S. H. (2012). High-pressure melting of metapelite and the formation of Ca-rich granitic melts in the Namche Barwa Massif, southern Tibet. *Gondwana Res.* 21 (1), 138–151. doi:10.1016/j.gr.2011.07.023
- Zeng, L. S., Gao, L. E., Tang, S. H., Hou, K. J., Guo, C. L., and Hu, G. Y. (2015). Eocene magmatism in the tethyan Himalaya, southern Tibet. *Geol. Soc. Lond. Spec. Publ.* 412, 287–316. doi:10.1144/sp412.8
- Zeng, L. S., Gao, L. E., Xie, K. J., and Jing, L. Z. (2011). Mid-Eocene high Sr/Y granites in the Northern Himalayan Gneiss Domes: Melting thickened lower continental crust. *Earth Planet. Sci. Lett.* 303, 251–266. doi:10.1016/j.epsl.2011.01.005
- Zeng, L. S., Liu, J., Gao, L. E., Xie, K. J., and Wen, L. (2009). Early Oligocene anatexis in the Yardoi gneiss dome, southern Tibet and geological implications. *Chin. Sci. Bull.* 54 (1), 104–112. doi:10.1007/s11434-008-0362-x
- Zeng, Y. C., Ducea, M. N., Xu, J. F., Chen, J. L., and Dong, Y. H. (2020). Negligible surface uplift following foundering of thickened central Tibetan lower crust. *Geology* 49 (1), 45–50. doi:10.1130/g48142.1
- Zhang, J. J., Santosh, M., Wang, X. X., Guo, L., Yang, X. Y., and Zhang, B. (2012). Tectonics of the northern Himalaya since the India-Asia collision. *Gondwana Res.* 21, 939–960. doi:10.1016/j.gr.2011.11.004

- Zhang, L. K., Li, G. M., Cao, H. W., Zhang, Z., Dong, S. L., Liang, W., et al. (2020). Activity of the south Tibetan detachment system: Constraints from leucogranite ages in the eastern Himalayas. *Geol. J.* 55 (7), 5540–5573. doi:10.1002/gj.3756
- Zhang, S. Q., Mahoney, J. J., Mo, X. X., Ghazi, A. M., Milani, L., Crawford, A. J., et al. (2005). Evidence for a widespread tethyan upper mantle with Indian-Ocean-Type isotopic characteristics. *J. Petrology* 46 (4), 829–858. doi:10.1093/ptrology/egi002
- Zhang, Z. M., Zhao, G. C., Santosh, M., Wang, J. L., Dong, X., and Shen, K. (2010). Late Cretaceous charnockite with adakitic affinities from the Gangdese batholith, southeastern Tibet: Evidence for Neo-Tethyan mid-ocean ridge subduction? *Gondwana Res.* 17 (4), 615–631. doi:10.1016/j.gr.2009.10.007
- Zheng, Y. C., Hou, Z. Q., Fu, Q., Zhu, D. C., Liang, W., and Xu, P. Y. (2016). Mantle inputs to Himalayan anatexis: Insights from petrogenesis of the Miocene Langkazi leucogranite and its dioritic enclaves. *Lithos* 264, 125–140. doi:10.1016/j.lithos.2016.08.019
- Zhu, D. C., Chung, S. L., Mo, X. X., Zhao, Z. D., Niu, Y. L., Song, B., et al. (2009a). The 132 Ma Comei-Bunbury large igneous province: Remnants identified in present-day southeastern Tibet and southwestern Australia. *Geology* 37 (7), 583–586. doi:10.1130/g30001a.1
- Zhu, D. C., Wang, Q., Cawood, P. A., Zhao, Z. D., and Mo, X. X. (2017). Raising the gangdese mountains in southern Tibet. *J. Geophys. Res. Solid Earth* 122, 214–223. doi:10.1002/2016jb013508
- Zhu, D. C., Wang, Q., Zhao, Z. D., Chung, S. L., Cawood, P. A., Niu, Y. L., et al. (2015). Magmatic record of India-Asia collision. *Sci. Rep.* 5, 14289. doi:10.1038/srep14289
- Zhu, D. C., Zhao, Z. D., Pan, G. T., Lee, H. Y., Kang, Z. Q., Liao, Z. L., et al. (2009b). Early cretaceous subduction-related adakite-like rocks of the Gangdese Belt, southern Tibet: Products of slab melting and subsequent melt-peridotite interaction? *J. Asian Earth Sci.* 34 (3), 298–309. doi:10.1016/j.jseas.2008.05.003
- Zindler, A., and Hart, S. (1986). Chemical geodynamics. *Annu. Rev. earth Planet. Sci.* 14, 493–571. doi:10.1146/annurev.ea.14.050186.002425
- Zong, K. Q., Chen, J. Y., Hu, Z. C., Liu, Y. S., Li, M., Fan, H. H., et al. (2015). *In-situ* U-Pb dating of uraninite by fs-LA-ICP-MS. *Sci. China Earth Sci.* 58 (10), 1731–1740. doi:10.1007/s11430-015-5154-y
- Zong, K. Q., Klemd, R., Yuan, Y., He, Z. Y., Guo, J. L., Shi, X. L., et al. (2017). The assembly of Rodinia: The correlation of early Neoproterozoic (ca. 900 Ma) high-grade metamorphism and continental arc formation in the southern Beishan Orogen, southern Central Asian Orogenic Belt (CAOB). *Precambrian Res.* 290, 32–48. doi:10.1016/j.precamres.2016.12.010